

1

2

3

4

Cosmic ray validation of electrode positions in small-strip thin gap chambers for the upgrade of the ATLAS detector

5

Lia Formenti

6

7

8

Department of Physics
McGill University, Montreal
October, 2021

9

10

11

12

13

A thesis submitted to
McGill University
in partial fulfillment of the
requirements of the degree of
Master of Science

¹⁵ Table of Contents

¹⁶	1	Introduction	1
¹⁷	2	High energy particle physics	4
¹⁸	2.1	The Standard Model	4
¹⁹	2.2	Beyond the Standard Model	6
²⁰	2.3	Studying high energy particle physics with accelerators	7
²¹	3	The LHC and the ATLAS experiment	9
²²	3.1	The Large Hadron Collider	9
²³	3.2	The High-Luminosity LHC	10
²⁴	3.3	The ATLAS experiment	12
²⁵	4	The New Small Wheels	17
²⁶	4.1	Motivation for the New Small Wheels	17
²⁷	4.2	Design of the NSWs	20
²⁸	4.3	Small-strip thin gap chambers	20
²⁹	4.4	sTGC Quadruplet Construction	23
³⁰	4.5	NSW alignment	24
³¹	5	Using cosmic muons to measure relative strip position offsets	27
³²	5.1	Cosmic rays	27
³³	5.2	Experimental setup	28

34	5.3 Data acquisition	29
35	5.4 Data preparation	30
36	5.4.1 Data quality cuts on electrode hits	30
37	5.4.2 Clustering and tracking	30
38	5.5 Relative local offsets	32
39	5.6 Systematic uncertainty	38
40	5.7 Discussion	40
41	6 Using x-rays to measure relative strip position offsets	41
42	6.1 Experimental setup	41
43	6.2 Data acquisition	43
44	6.3 Data preparation	43
45	6.4 Measuring local offsets	43
46	6.5 Measuring relative local offsets	45
47	7 Comparing cosmic muon and x-ray relative strip position offsets	48
48	7.1 Results	48
49	7.2 Discussion	53
50	7.3 Next steps	54
51	8 Summary and outlook	56
52	References	57
53	APPENDICES	64
54	A Cluster position uncertainty	65
55	B Analysis statistics	67

56	C Analysis systematics	69
57	C.1 Residual distribution fit function	69
58	C.2 Cosmic muon data collection voltage	72
59	C.3 Cluster fit algorithm	73
60	C.4 Differential non-linearity	74
61	D Printable plots	77

Abstract

63 The Large Hadron Collider (LHC) is used to generate subatomic physics processes at the
64 energy frontier to challenge our understanding of the Standard Model of particle physics.
65 The particle collision rate at the LHC will be increased up to seven times its design value in
66 2025-2027 by an extensive upgrade program. The innermost endcaps of the ATLAS muon
67 spectrometer consist of two wheels of muon detectors that must be replaced to maintain
68 the muon momentum resolution in the high-rate environment. The so-called New Small
69 Wheels (NSWs) are made of two detector technologies: micromegas and small-strip thin gap
70 chambers (sTGCs). The sTGCs are gas ionization chambers that hold a thin volume of gas
71 between two cathode boards. One board is segmented into copper readout strips of 3.2 mm
72 pitch that are used to precisely reconstruct the coordinate of a passing muon. Modules of
73 four sTGCs glued together into quadruplets cover the NSWs. Quadruplets were designed
74 to achieve a 1 mrad angular resolution to fulfill the spectrometer's triggering and precision
75 tracking requirements. To achieve the required angular resolution the absolute position of
76 the readout strips must be known in the ATLAS coordinate system to within 100 μm . At
77 McGill University, the performance of sTGC quadruplets was characterized using cosmic ray
78 data before being sent to CERN, where the charge profile left by x-rays is used to measure
79 the offset of the strip patterns with respect to nominal at a limited number of points on
80 the surface of each quadruplet. The x-ray strip position measurements have acceptable but
81 limited precision and do not span the whole area of the strip layers. Given the importance of
82 knowing the absolute position of each readout strip to achieve the performance requirements
83 of the NSWs, the x-ray method must be validated by an independent method. Cosmic ray
84 data is used to characterize the relative alignment between layers and validate the x-ray
85 method.

Résumé

Le grand collisionneur des hadrons (LHC) utilise des collisions de protons afin de générer des processus de la physique subatomique à la frontière même de la haute énergie, et ceci afin de tenter remettre en cause le modèle standard de la physique des particules. Le taux des collisions entre protons au LHC sera augmenté jusqu'à sept fois le taux nominal d'ici 2025-2027 à l'aide d'un programme de mise à niveau de grande envergure. Une partie du spectromètre à muons du détecteur ATLAS consistant de deux roues de détecteurs de muons doit être remplacée afin de maintenir la résolution sur l'inertie des muons à haut taux de collision. Appelées les Nouvelles Petites Roues (NSWs), elles utilisent deux technologies de détection différentes: des chambres micromegas et des chambres à petites bandes et à intervalles fins (sTGCs). Les sTGCs sont des chambres d'ionisation de gaz, qui contiennent un volume très fin de gaz entre deux panneaux cathodiques. Un panneau est segmenté avec de petites bandes en cuivre en pente de 3.2 mm. Ceux-ci détectent le signal laissé par des muons et permettent la mesure précise des coordonnées spatiales des muons qui traversent le détecteur. Des modules de quatre sTGCs collés ensemble en quaduplets couvrent la superficie des NSWs. Ces quadruplets ont été conçus afin de permettre une résolution angulaire de 1 mrad, et de satisfaire les exigences des systèmes de déclenchement et de mesures de précision. Afin d'atteindre cette résolution angulaire il faut que la position absolue de chaque bande soit connue au sein du détecteur ATLAS avec une précision d'au moins 100 μ m. À l'Université de McGill, la performance des quadruplets a été caractériser avec des rayons cosmiques avant leur envoi au CERN, où le profil des charges laissé par des rayons X est utilisé pour mesurer le déplacement du motif des bandes par rapport à leur emplacement nominal. Ceci est fait à un nombre de positions limité sur la surface des quadruplets. Ces déplacements, mesurés par les rayons X, ont une précision acceptable mais limitée et ne couvrent pas la région entière des panneaux. Étant donné l'importance de la caractérisation précise de la position absolue de chaque bande afin de réaliser les exigences de rendement des NSWs, une méthode indépendante de validation de la méthode des rayons X est requise. Les données recueillies avec les rayons cosmiques sont utilisées pour caractériser l'alignement relatif entre les panneaux et valider la méthode des rayons-X.

Acknowledgements

- 116 Experimental particle physics projects are never done alone. I am grateful to have been
117 working with the ATLAS Collaboration for two years now.
- 118 Thank you to Dr. Brigitte Vachon for her guidance throughout this project and for editing
119 this thesis. I am consistently amazed by her ability to jump into the details of my project
120 and discuss them with me.
- 121 Thanks also to Dr. Benoit Lefebvre, who collected some of the data used in this thesis, wrote
122 several software tools I used to analyze the data and advised me several times throughout
123 this project.
- 124 Thank you to my labmates at McGill University, Dr. Tony Kwan, Kathrin Brunner, John
125 McGowan and Charlie Chen. Kathrin taught me mechanical skills that I will apply elsewhere.
126 Tony, manager of the laboratory, created the most encouraging, trusting and productive work
127 environment I have ever been apart of.
- 128 Thank you to the friends I can call on at anytime, and thank you to my family whose
129 constant support makes every step possible.

Contribution of authors

I, the author, was involved in collecting the cosmic ray data from September 2019 - March 2021. I did not design the cosmic ray testing procedure nor write the data preparation software, but I participated in using the software to analyze cosmic ray results. In the thesis, the terms “clustering,” “local offset” and “relative local offset” are defined. Cosmic ray clustering was done in the data preparation software, but I redid the fit afterwards to explore sensitivity to the fit algorithm. With help from Dr. Lefebvre and Dr. Vachon, I helped design the software that calculated the relative local offsets from cosmic ray data. I wrote that software on my own. I was not involved in the design, data collection, data preparation or analysis of the x-ray data. I also was not involved in creating an alignment model from the x-ray data. I used the x-ray local offsets calculated using x-ray data analysis software to calculate relative local offsets with x-rays. I did the comparison between the x-ray and cosmic ray data.

I hereby declare that I am the sole author of this thesis. This is a true copy of the thesis, including any required final revisions, as accepted by my examiners.

¹⁴⁵

Chapter 1

¹⁴⁶

Introduction

¹⁴⁷ The Standard Model (SM) is a theoretical framework that describes experimental observa-
¹⁴⁸ tions of particles and their interactions at the smallest distance scales; however, the questions
¹⁴⁹ the SM does not address motivate more experimentation.

¹⁵⁰ Accelerators collide particles to generate interactions that can be recorded by detectors
¹⁵¹ for further study. Detectors measure the trajectory and energy of all secondary particles
¹⁵² produced in collisions to understand the interaction. The Large Hadron Collider (LHC) [1]
¹⁵³ at CERN is the world’s most energetic particle accelerator. Its energy makes it a unique
¹⁵⁴ tool to study elementary particles and their interactions in an environment with conditions
¹⁵⁵ similar to what would have existed in the early universe. If study at the energy frontier is
¹⁵⁶ to continue, the LHC must go on.

¹⁵⁷ After 2025, the statistical gain in running the LHC further without significant increase in
¹⁵⁸ beam intensity will become marginal. The High Luminosity Large Hadron Collider (HL-
¹⁵⁹ LHC) project [2] is a series of upgrades to LHC infrastructure that will allow the LHC
¹⁶⁰ to collect approximately ten times more data than in the initial design by \sim 2030. The
¹⁶¹ increase in LHC beam intensity will result in a large increase in collision rate that will make
¹⁶² accessible and improve statistics on several measurements of interest [3], many only possible
¹⁶³ at the LHC and the energy frontier. The increase in beam intensity will also increase the
¹⁶⁴ level of background radiation, requiring major upgrades to the experiments used to record
¹⁶⁵ the outcomes of the particle collisions.

¹⁶⁶ The ATLAS experiment [4] is one of the LHC’s general-purpose particle detector arrays, po-
¹⁶⁷ sitioned around one of the collision points of the LHC. During the 2019-2022 Long Shutdown
¹⁶⁸ of the LHC, the most complex upgrade of the ATLAS experiment is the replacement of the
¹⁶⁹ small wheels of the muon spectrometer with the so-called New Small Wheels (NSWs) [5].

170 The detector upgrade addresses both the expected decrease in hit efficiency of the precision
171 tracking detectors and the high fake trigger rate expected in the muon spectrometer at the
172 HL-LHC. The NSWs are made of two different detector technologies: micromegas and small-
173 strip thin gap chambers (sTGCs). Micromegas are optimized for precision tracking while
174 sTGCs are optimized for rapid triggering, although each will provide complete coverage and
175 measurement redundancy over the area of the NSWs. Eight layers each of sTGCs cover the
176 NSWs. Practically, countries involved in detector constructor created quadruplet modules of
177 four sTGCs glued together that were arranged and installed over the area of the NSWs once
178 they arrived at CERN. Teams across three Canadian institutions built and characterized 1/4
179 of all the required sTGCs.

180 The sTGCs are gas ionization chambers that consist of a thin volume of gas held between two
181 cathode boards. One board is segmented into strip readout electrodes of 3.2 mm pitch. The
182 position of the particle track in the precision coordinate can be reconstructed from the strip
183 signals [5]. The sTGCs achieved the design track spatial resolution in the precision coordinate
184 of less than 100 μm per detector plane that will allow them to achieve a 1 mrad track angular
185 resolution using the 8 layers of sTGC on the NSW [6, 5]. The NSW measurement of the
186 muon track angle will be provided to the ATLAS trigger and used to reject tracks that do
187 not originate from the interaction point [5].

188 The precise measurement of a muon track angle depends on knowing the position of each
189 readout strip within the ATLAS coordinate system. To achieve this, the position of specific
190 locations on the surface of sTGC quadruplets will be monitored by the ATLAS alignment
191 system to account for time-dependent deformations [5]. Within a quadruplet module, the
192 strip positions could have been shifted off of nominal by non-conformities of the strip pattern
193 etched onto each cathode boards [7] and shifts between strip layers while gluing sTGCs into
194 quadruplets.

195 An x-ray gun was used to measure the offset of strips from their nominal position at the
196 locations that will be monitored by the ATLAS alignment system thereby providing, locally,
197 an absolute “as-built” strip position within the ATLAS coordinate system. Estimates of the
198 “as-built” positions of every readout strip are obtained by building an alignment model from
199 the available x-ray measurements [8].

200 The technique of measuring the “as-built” strip positions using x-ray data has never been
201 used before and must be validated. This thesis describes the use of cosmic muon data,
202 recorded to characterize the performance of each Canadian-made sTGC module, to validate
203 the x-ray strip position measurements. A description of how this work fits within the overall
204 alignment scheme of the NSW is also presented.

205 Chapter 2 gives a brief overview of high energy particle physics necessary to understand the
206 physics motivation of the HL-LHC and NSW upgrades. Chapters 3 and 4 present additional

207 details on the LHC, ATLAS, the NSWs, and sTGCs. In Chapter 5, the cosmic ray testing
208 procedure and how the position of the strips can be probed with cosmics data is presented.
209 Chapter 6 introduces the x-ray method, and in Chapter 7, the x-ray offsets are validated
210 with cosmic muon data. The thesis concludes with a summary and outlook in Chapter 8.

²¹¹ Chapter 2

²¹² High energy particle physics

²¹³ Particle physics aims to study the elementary constituents of matter. Understanding the fundamental building blocks and how they interact provides insight into how the early universe evolved to the forms of matter we observe today. This chapter introduces general concepts in particle physics relevant to understanding the physics goals of the High-Luminosity LHC (HL-LHC) and NSWs upgrade.

²¹⁸ The information on particle physics and the SM presented here is rather general; the interested reader is referred to [9, 10, 11] for more information.

²²⁰ 2.1 The Standard Model

²²¹ The Standard Model (SM) is a theoretical framework developed in the early 1970's that describes the observed elementary particles and their interactions. It is built on a collection of quantum field theories and has been remarkably successful at predicting experimental observations, including but not limited to the existence of the top quark [12], the tau neutrino [13] and the Higgs boson [14, 15].

²²⁶ The known elementary particles described by the SM are represented in Figure 2.1. There are 12 matter particles (six quarks and six leptons), 4 force-mediating particles, and the Higgs boson. Each matter particle also has an anti-matter particle pair with the same mass but opposite charge, not represented in Figure 2.1. The different forces of nature are understood to be the result of the exchange of force-mediating particles between interacting (coupled) particles. Photons are mediators of the electromagnetic force, W⁺/- and Z bosons are mediators of the weak force, and gluons are mediators of the strong force. At high

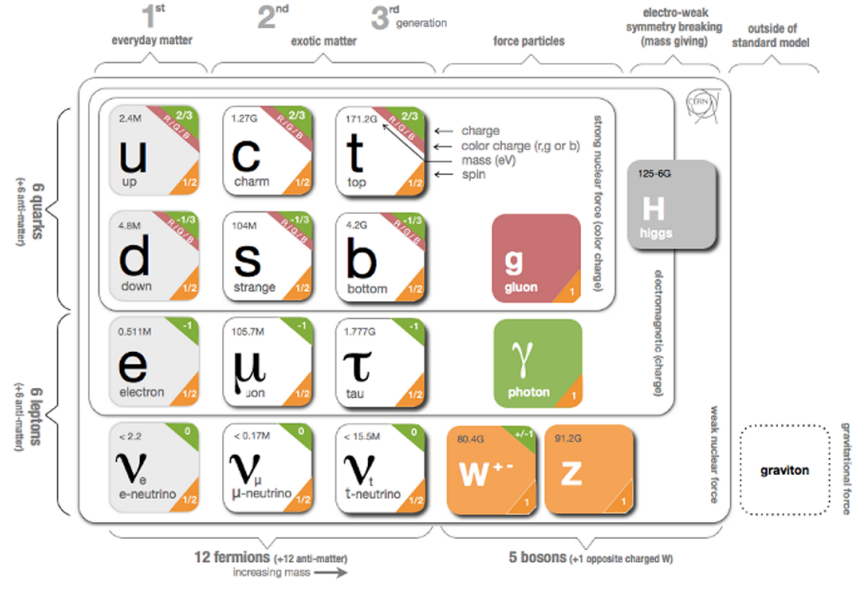


Figure 2.1: Schematic diagram of all elementary particles in the SM. Particles are grouped according to their properties and the forces through which they interact with other particles [16].

233 energy, the SM describes the electromagnetic and weak forces as stemming from a unified
 234 electroweak force. The Higgs boson field interacts with the particles mediating the unified
 235 electroweak force to distinguish the weak and electromagnetic forces from each other at lower
 236 energies and give particles (except neutrinos) a mass. This is called electroweak symmetry
 237 breaking.

238 Quarks are matter particles that are sensitive to all forces; notably they are the only particles
 239 sensitive to the strong force. Protons and neutrons are made up of quarks and gluons, and the
 240 strong force is responsible for their existence and mutual attraction into nuclei [17]. Leptons
 241 are particles not sensitive to the strong force. Charged leptons include the electron, which
 242 once part of atoms is responsible for chemistry. Of particular importance for this thesis is
 243 the charged lepton called a muon. It is like the electron but its mass is ~ 200 times larger
 244 than that of the electron. Muons have a lifetime of $2.2 \mu\text{s}$ [11] and decay predominantly as
 245 $\mu \rightarrow e^- \bar{\nu}_e \nu_\mu$. Neutrinos are neutral, almost massless leptons that only interact through the
 246 weak force.

247 Common matter is made up of the lightest constituents of the SM: up and down quarks,
248 electrons and photons. The other particles are produced in high-energy environments but
249 then decay to the lightest constituents. Such high energy environments include the condi-
250 tions present in the early universe [18], astrophysical sources, and particle accelerators. The
251 presence of the particles of the SM at the beginning of the Universe means that their inter-
252 actions and decays are fundamental for the study of the evolution of the early universe [18].
253 Many high energy astrophysical sources, like supernovae, generate particles that rain down
254 on Earth as cosmic rays [19]. Particle accelerators have been built to create controlled en-
255 vironments of high-rate, high-energy particle collisions at high energy where the production
256 and decay of elementary particles can be directly studied.

257 2.2 Beyond the Standard Model

258 Despite its success at describing most experimental observations to date, there is ample
259 evidence that the SM is not a complete description of natural phenomena at the smallest
260 scales. For example, the SM has a large number of free parameters, the values of which have
261 to be fine-tuned to fit experimental observations. This is part of the so-called “naturalness”
262 problem.

263 Furthermore, the SM provides no explanation for several open questions in particle physics.
264 First, neutrinos in the SM are assumed to be massless and do not gain mass in the same way
265 as the other particles. However, neutrino were confirmed to change between their different
266 flavours in 2013 [20], which can only occur if neutrinos do have mass [21]. The neutrino
267 mass requires physics beyond the standard model [22]. Second, several astrophysical and
268 cosmological measurements suggest the presence of “dark matter” making up 85 % of the
269 matter content of the universe [23]. The nature of dark matter is unknown and so far there
270 is no SM explanation [24]. Third, the SM does not explain the origin and nature of the
271 matter-antimatter asymmetry that produced our matter-dominated universe. Finally, the
272 SM does not include a description of gravity.

273 Theoretical extensions beyond the Standard Model (BSM) aim to address some of these
274 questions, often predicting existence of yet-unseen elementary particles or physics phenomena
275 beyond those predicted by the SM. These hypothetical new physics phenomena or new
276 particles can be searched for at particle accelerators.

277 **2.3 Studying high energy particle physics with accelerators**

278

279 In particular, particle accelerators of increasingly higher energy have a long history of enabling the discovery of predicted particles. These include, for example, the discovery of 280 the W [25, 26] and Z bosons [27, 28], the top quark [29, 30], and most recently, the Higgs 281 boson [31, 32]. The discovery of the Higgs boson marked the completion of the SM as it is 282 known today.

284 Based on the established success of the SM, there are two approaches to particle physics 285 research. One approach is to search for the existence of new physics phenomena predicted 286 to exist in BSM theories and the other is to test the validity of the SM to a high degree of 287 accuracy to search for flaws in the model. Standard Model predictions are generally expressed 288 in terms of the probability of a specific physics process to occur, expressed as a cross section 289 in units of barns (with 1 barn = 10^{-28} m²). As an example, Figure 2.1 shows a summary 290 of cross section measured for different physics processes using the ATLAS experiment and 291 their comparison with the predictions of the SM. Most cross section measurements agree 292 well within one standard deviation with the SM predictions.

293 Particle accelerators provide a controlled and high-collision rate environment that makes 294 them ideal places to search for new physics phenomena and to carry out systematic tests of 295 the SM. The LHC is the highest energy collider in the world so it can access physics that 296 no other accelerator can. A description of the LHC and the ATLAS detector are provided 297 in the next chapter.

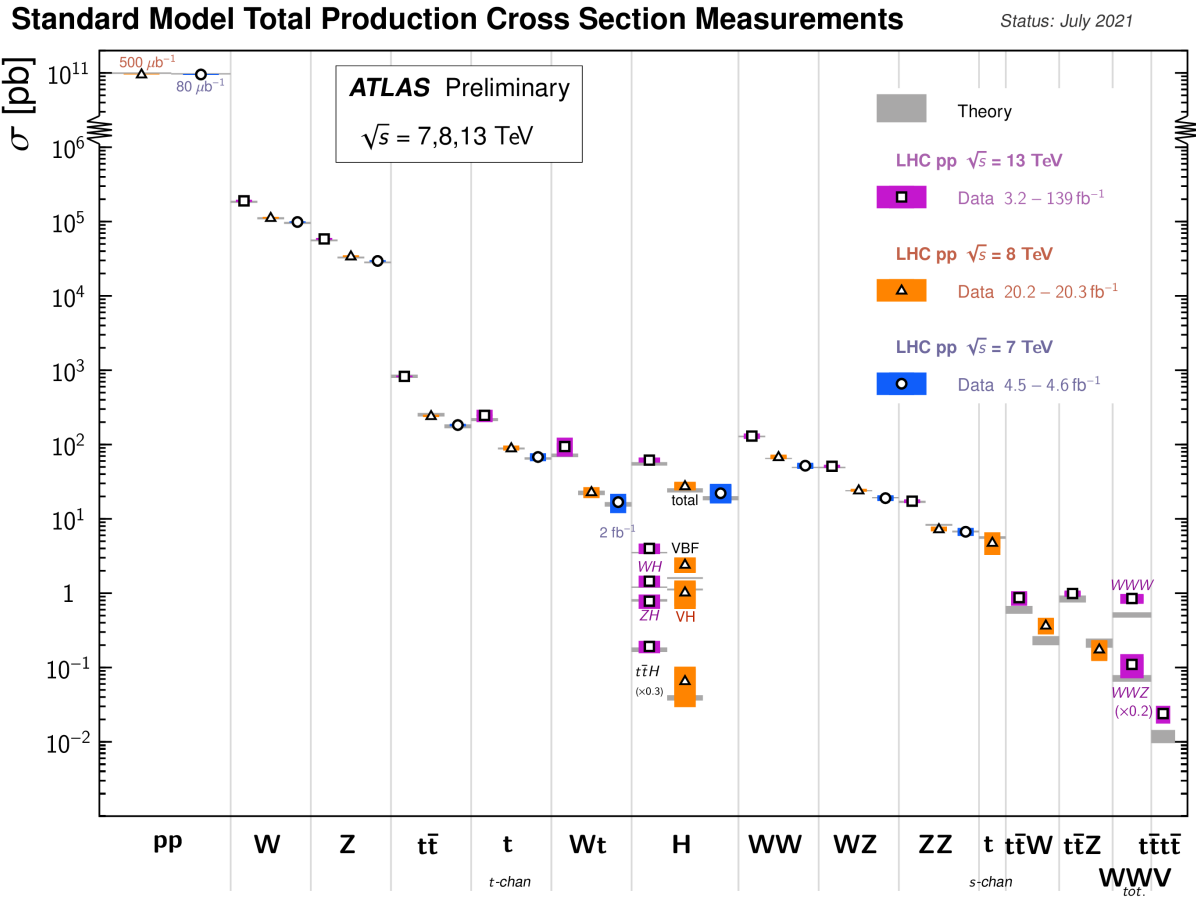


Figure 2.2: Production cross sections of different final states measured by the ATLAS experiment at the LHC. Comparison with the SM theory predictions is also shown [33].

298 **Chapter 3**

299 **The LHC and the ATLAS experiment**

300 The Large Hadron Collider (LHC) is the world’s most energetic particle accelerator and the
301 ATLAS experiment is used to record the results of particle collisions at the LHC. In this
302 chapter, details about both that are necessary to understand the High-Luminosity LHC (HL-
303 LHC) upgrade project and the ATLAS experiment’s New Small Wheels (NSWs) upgrade
304 are presented.

305 **3.1 The Large Hadron Collider**

306 The LHC is an accelerator 27 km in circumference and located \sim 100 m underground at
307 the CERN laboratory near Geneva, Switzerland [1]. It has two beam pipes within which
308 bunches of protons counter-circulate before being collided in the center of one of four major
309 experiments, such as the ATLAS experiment (discussed in Section 3.3). Protons are guided
310 on the circular trajectory using 1232 superconducting dipole magnets capable of a maximum
311 field of 8.33 T. Radio-frequency accelerating cavities are used to accelerate protons to a
312 the maximum design energy of 7 TeV [34]. During LHC Run-1 (2011-2012), protons were
313 collided at a collision center-of-mass energy of 7 TeV and 8 TeV [35]. During LHC Run-2
314 (2015-2018), the center-of-mass energy of proton collisions was increased to 13 TeV [36],
315 close to the maximum design value of 14 TeV [34]. It is not actually the protons that
316 interact, but the constituent quarks and gluons that each carry some fraction of the energy
317 and momentum of the collisions.

318 **Luminosity**

319 The number of proton-proton interactions generated by the LHC directly affects the statistics

available to make measurements of interaction cross sections. Predicting the number of proton-proton interactions requires defining a metric called luminosity [11]. The luminosity of a particle collider is the number of particles an accelerator can send through a given area per unit time. It is calculated from the measurable quantities in Equation 3.1:

$$\mathcal{L} = \frac{f N_1 N_2}{4\pi\sigma_x\sigma_y}, \quad (3.1)$$

where f is the frequency of the bunch crossings (25 ns), N_1 and N_2 are the number of protons in each bunch ($\sim 10^{11}$ protons / bunch), and σ_x and σ_y are the RMS of the spatial distributions of the bunch. Therefore, luminosity is a property of accelerator beams, which are set by the capabilities of the accelerator. The design luminosity of the LHC was $10^{34} \text{ cm}^{-2}\text{s}^{-1}$. The units of luminosity are an inverse area; multiplying the luminosity by the cross section of a given process gives the expected rate for that process.

Integrating the *instantaneous* luminosity (Equation 3.1) over a period of data collection time gives the integrated luminosity,

$$L = \int \mathcal{L}(t) dt \quad (3.2)$$

which is related to the total number of interactions. In this way, the luminosity is the link between the accelerator and the statistical power of measurements to be made with the data collected. So far, the LHC provided an integrated luminosity of 28.26 fb^{-1} in Run-1 [35] and 156 fb^{-1} in Run-2 [36].

3.2 The High-Luminosity LHC

At the end of the LHC program in 2025, the statistical gain on measurements in running the LHC further will become marginal. The HL-LHC [2] project consists of the upgrade of LHC infrastructure to achieve a nearly ten fold increase in instantaneous luminosity, thereby improving measurement statistics as well. Also, some systems will need repair and replacement to operate past ~ 2020 . The LHC will continue to be the most energetic accelerator in the world for years to come and is the only accelerator with enough energy to directly produce the Higgs boson and top quarks. Therefore, the European Strategy for Particle Physics made it a priority “to fully exploit the physics potential of the LHC” with “a major luminosity upgrade” [37]. The goal is for the HL-LHC to provide an integrated luminosity of 3000 fb^{-1} in the 12 years following the upgrade. The luminosity actually



Figure 3.1: The LHC/HL-LHC timeline [38]. The integrated luminosities collected and projected for each run of the LHC are shown in blue boxes below the timeline and the center of mass energy of the collisions is shown in red above the timeline. The top blue arrow labels the run number. The acronym “LS” stands for “long shutdown” and indicates periods where the accelerator is not operating. During the shutdowns, upgrades to the LHC and the experiments are taking place. This timeline was last updated in January, 2021, and reflects changes in the schedule due to the ongoing pandemic.

347 achieved will depend on a combination of technological advances and upgrades in progress
 348 that affect the factors contributing to luminosity defined in Equation 3.1 [2]. Figure 3.1
 349 shows the projected schedule of the HL-LHC upgrades and operation [38].

350 One of the most anticipated measurements at the HL-LHC is the value of the triple-Higgs
 351 coupling. Measuring the coupling will allow the determination of the shape of the Higgs
 352 potential responsible for electroweak symmetry breaking. Any discrepancy with respect to
 353 the SM prediction will show that there must be other sources of electroweak symmetry
 354 breaking, and hence physics phenomena beyond the SM. The LHC is the only accelerator
 355 where the Higgs boson can be produced directly so it is the only place where the triple-Higgs
 356 coupling could be measured. The HL-LHC upgrade is required to produce a significant
 357 sample of Higgs produced in pairs to make a statistically meaningful measurement [3, 39].

358 Accordingly, detector sensitivity to various Higgs decays will be important at the HL-LHC.

359 3.3 The ATLAS experiment

360 The ATLAS experiment [4] was designed to support all the physics goals of the LHC. It is
361 44 m long and 25 m in diameter, and weighs 7000 tonnes. The ATLAS experiment is centered
362 around one of the LHC's interaction points (a place where the beams collide). As shown
363 schematically in Figure 3.2, ATLAS consists of an array of particle detector subsystems
364 arranged concentrically around the beam pipe. The ATLAS experiment is cylindrical because
365 it aims to provide 4π coverage around the interaction point. In reference to the cylindrical
366 geometry of the experiment, it is helpful to separate the subsystems of ATLAS into the
367 so-called "barrel" and "endcap"/"forward" regions.

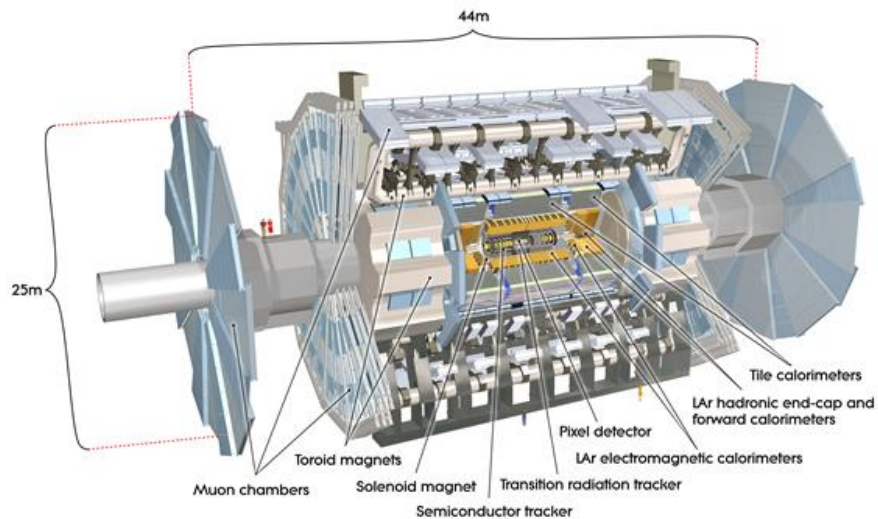


Figure 3.2: Schematic diagram of the ATLAS experiment, with the various detector subsystems labelled [4].

368 For analysis purposes, a spherical coordinate system is defined. The azimuthal angle ϕ is
369 measured around the beampipe and the polar angle θ is measured from the beam pipe. The
370 polar angle is more often expressed in terms of pseudo-rapidity, defined as $\eta = -\ln \tan(\theta/2)$.
371 Pseudo-rapidity values vary from 0 (perpendicular to the beam) to $\pm\infty$ (parallel to the
372 beam, defined as the z-direction) and is an approximation to the rapidity of a particle when
373 its momentum is much greater than its mass. It is useful to describe the direction of outgoing

374 particles in proton-proton collisions because differences in rapidity are invariant to a Lorentz
375 boost along the beam direction.

376 The ATLAS experiment provides identification and kinematic measurements for each particle
377 created after the initial collision, which is done by assembling offline the information recorded
378 by each subsystem. With this information, signatures of processes of interest can be identified
379 and studied. An overview of the main ATLAS subsystems is given below.

380 **The inner detector**

381 The inner detector [40, 41] (Figure 3.3) is for precise measurements of charged particle
382 trajectories, measurement of primary and secondary interaction vertices and assistance in the
383 identification of electrons. A 2 T solenoid with field parallel to the beam bends the trajectory
384 of outgoing charged particles. A measurement of the bending radius of each charged particle
385 provides information about its momentum. The innermost part of the inner tracker is made
386 of high-resolution semiconductor pixel and strip detectors while the outermost part is made
387 of straw-tubes. The straw tubes are used in the trajectory measurements but they are
388 also interspersed with material designed to enhance the creation of transition radiation.
389 Transition radiation occurs when a highly relativistic charged particle traverses a material
390 boundary [42]. The amount of transition radiation emitted by a charged particle is detected
391 by the straw-tubes and is used to identify electrons.

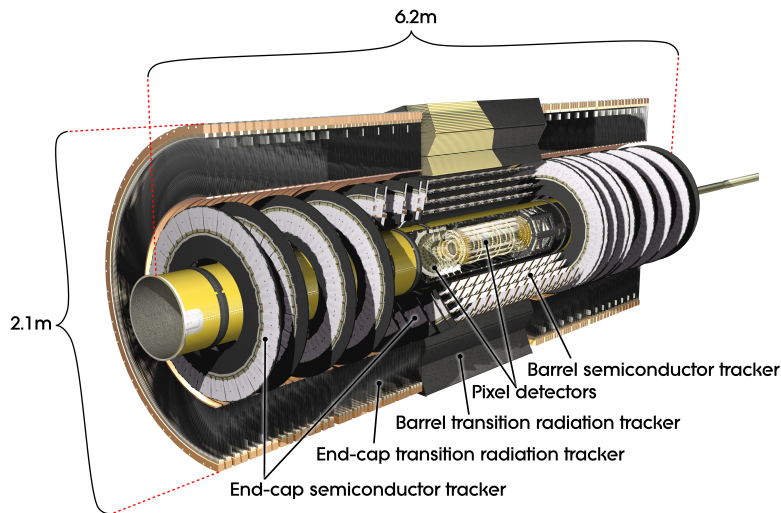


Figure 3.3: Schematic diagram of the ATLAS experiment's inner detector, with the different segments and the technology used labeled [4].

392 **Calorimetry system**

393 Electromagnetic and hadronic sampling calorimeter units are used to record the energy
394 of electrons, photons and jets¹. A combination of liquid-argon (LAr) electromagnetic and
395 hadronic calorimeters [43] and tile-scintillator hadronic calorimeters [44] cover the rapidity
396 range $|\eta| < 4.9$, as shown in Figure 3.4.

397 Sampling calorimeters have alternating layers of dense material and material that can mea-
398 sure the amount of ionization by charged particles. The dense material causes incoming
399 charged particles to shower into lower energy particles and deposit their energy in the sen-
400 sitive volume. Only muons and neutrinos are known to pass the calorimeters to the muon
401 spectrometer without being absorbed.

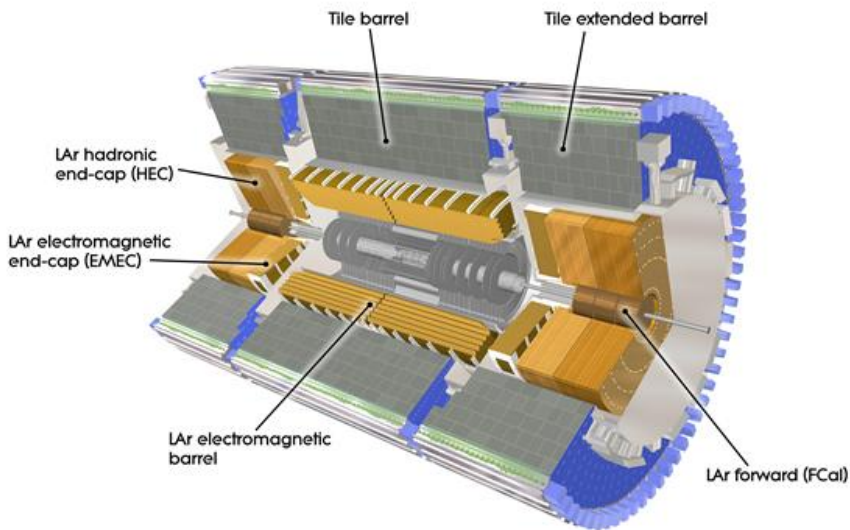


Figure 3.4: Schematic diagram of the ATLAS calorimeter system, with the different segments and the technology used labeled [4].

402 **Muon spectrometer**

403 The muon spectrometer [45] consists of multiple layers of tracking chambers embedded in
404 a 2 T magnetic field generated by an air-core superconducting toroid magnet system. Fig-
405 ure 3.5a shows a schematic diagram of the layout of the different chambers and of the toroid

¹When quarks or gluons are expelled in a high energy collision, they create collimated groups of hadrons called jets because they carry a charge called “colour”, and nature only allows “colourless” combinations to exist [42].

406 magnets [4]. The trajectory of a muon is reconstructed from the information recorded by
 407 the different types and layers of tracking chambers. The amount of bending in the magnetic
 408 field provides a measure of the muon's momentum. In the barrel section of ATLAS, the
 409 toroidal magnetic field is created by eight coils bent into the shape of a "race-track" and
 410 symmetrically arranged around the beampipe. In the forward region, two end-cap toroids,
 411 each with eight smaller racetrack-shaped coils arranged symmetrically around the beam pipe
 412 are inserted in the ends of the barrel toroid [46].

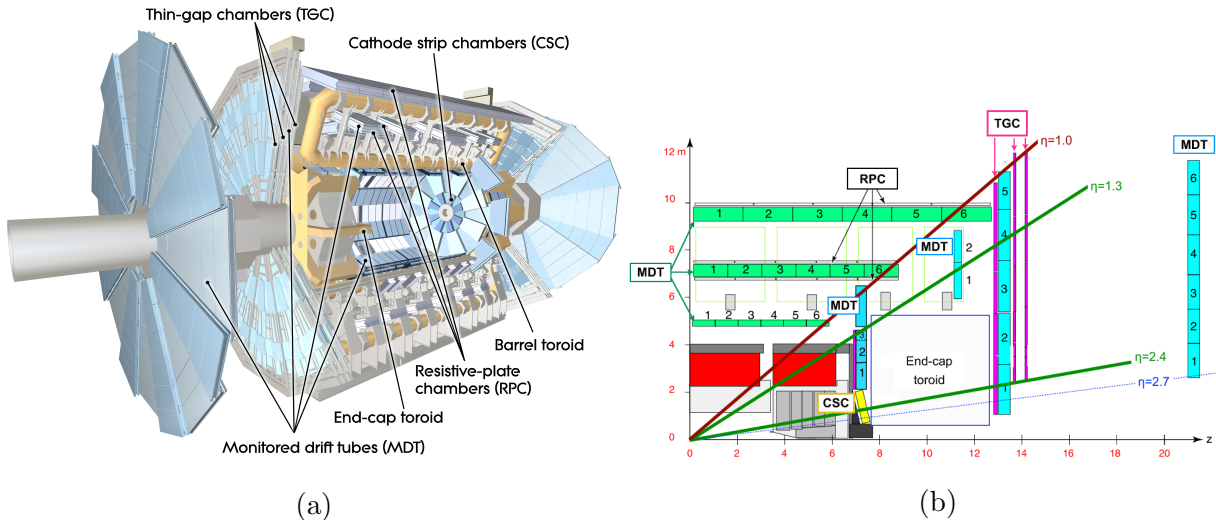


Figure 3.5: Schematic diagram of the ATLAS muon spectrometer. Figure (a) shows a 3D projection of the system with the different types of chambers and different parts of the toroidal magnet system labeled [4]. Figure (b) shows a projection of one quarter of the muon spectrometer, with the interaction point in the bottom left corner. The small wheel is just left of the end cap toroid, the big wheel is to its right, and the outer wheel is the rightmost structure [47].

413 The muon spectrometer is separated into detectors used for precision offline tracking and
 414 for triggering purposes. Three layers of monitored drift tubes (MDTs) or cathode strip
 415 chambers (CSCs) are used for tracking. The position of the muon track in each of the three
 416 layers allows reconstruction of the bent trajectory of a muon and hence its momentum. To
 417 satisfy the muon spectrometer target momentum resolution of $\Delta p_T/p_T < 1 \times 10^{-4} p / \text{GeV}$
 418 for $p_T < 300 \text{ GeV}$ and a few percent for lower p_T muons, the MDTs and CSCs were designed
 419 to achieve a spatial resolution of $50 \mu\text{m}$ each. Accordingly, an optical alignment system was
 420 designed to monitor and correct for chamber positions [45, 48].

421 Resistive plate chambers (RPCs) are used for triggering in the barrel and thin-gap chambers

422 (TGCs) are used for triggering in the endcaps. The positions of each type of chamber
423 are sketched in Figure 3.5b. The endcap section of the muon spectrometer consists of three
424 sections, the small wheel, big wheel, and outer wheel – ordered by proximity to the interaction
425 point. In Run-1, low (high) p_T muons were triggered on if two (three) of the RPC or TGC
426 layers around the big wheel fired in coincidence, for the barrel and endcaps respectively [49].
427 After Run-1 it was discovered that up to 90% of the triggers in the endcap were fake, caused
428 by background particles generated in the material between the small wheel and the big
429 wheel [5]. To reduce the fake rate in Run-2, the TGCs on the inside of the small wheel also
430 had to register a hit. The added condition reduced the trigger rate by 50% in the range $1.3 < |\eta| < 1.9$ [50]. The effectiveness of the solution was limited since the $|\eta|$ -range of the small
431 wheel TGCs was limited to $1.0 < |\eta| < 1.9$ and the spatial resolution of the small wheel
432 TGCs is coarse [5].

434 **Trigger system**

435 It would be impossible to record all the data from bunch crossings every 25 ns, corresponding
436 to a rate of ~ 40 MHz. The ATLAS experiment has a multi-level trigger system to select
437 events of interest for permanent storage. The Level-1 (L1) hardware trigger [49] uses partial-
438 granularity information from the muon spectrometer and calorimeters to trigger on high p_T
439 muons, electrons, jets, missing transverse energy, and τ decaying to hadrons. After Run-3
440 an upgrade of the trigger system will allow a maximum trigger rate of 1 MHz with a latency
441 of 10 μ s [51], but for now the working limits are a rate of 100 kHz [50] and 2.5 μ s [49].

442 The L1 trigger is used to define regions of interest that are fed into the software high level
443 trigger (HLT) [52], in which the full granularity of the muon spectrometer and calorimeter
444 are used with information from the inner detector to reduce the trigger rate to 1 kHz. Events
445 that satisfy at least one of the L1 and HLT trigger criteria are recorded to permanent storage
446 for offline analysis.

447

448 With the foreseen increase in luminosity at HL-LHC, it is a priority to upgrade the ATLAS
449 detector to further reduce the muon trigger fake rate in the forward region. The New Small
450 Wheels being commissioned to replace the original ATLAS muon small wheels will address
451 this challenge.

452 **Chapter 4**

453 **The New Small Wheels**

454 **4.1 Motivation for the New Small Wheels**

455 The hit rate of all detector systems will significantly increase during HL-LHC operation
456 because of the increase in luminosity. The increased rate presents a challenge for both the
457 tracking and triggering capabilities of the muon spectrometer [5].

458 In terms of precision tracking, the maximum hit rate in the MDTs is expected to reach above
459 300 kHz by the end LHC operation. At this rate, the hit efficiency of MDTs decreases by
460 35%, mostly due to the long dead-time of the chambers. Losing hits in the small wheel will
461 reduce the high p_T muon momentum resolution. The decrease in resolution will affect the
462 ability to search for, for example, the decay of hypothetical heavy bosons (W' , Z') or other
463 hypothetical particles beyond the SM [3].

464 Already during LHC Run-2 operation, the forward muon trigger system had to cope with a
465 very high fake rate, even with the inclusion of TGC data from the small wheel as part of the
466 trigger criteria. At the luminosity expected in Run-3, it is estimated that 60 kHz out of the
467 maximum L1 trigger bandwidth of 100 kHz would be taken up by forward muon triggers.
468 To address this challenge, a possible solution would be to raise the minimum p_T threshold
469 from 20 GeV to 40 GeV. However, this would have an adverse impact on the ability to study
470 several physics processes of interest that depend on low p_T muons, particularly the Higgs
471 decay to two muons, the Higgs decay to two tau leptons and hypothetical particle decays
472 beyond the SM [5].

473 The NSWs will address both of these problems. They will be made of precision tracking
474 chambers suitable for the expected hit rates during the HL-LHC and triggering chambers
475 capable of 1 mrad track angular resolution. The idea behind the design triggering capability



Figure 4.1: A schematic diagram of a quarter cross section of the ATLAS muon spectrometer, with the interaction point (IP) in the bottom left corner. Three possible tracks are labeled. Ideally, track A would be triggered on while track B and C discarded. With the old small wheel, all three tracks would be recorded. With the NSW, only track A would be recorded [5].

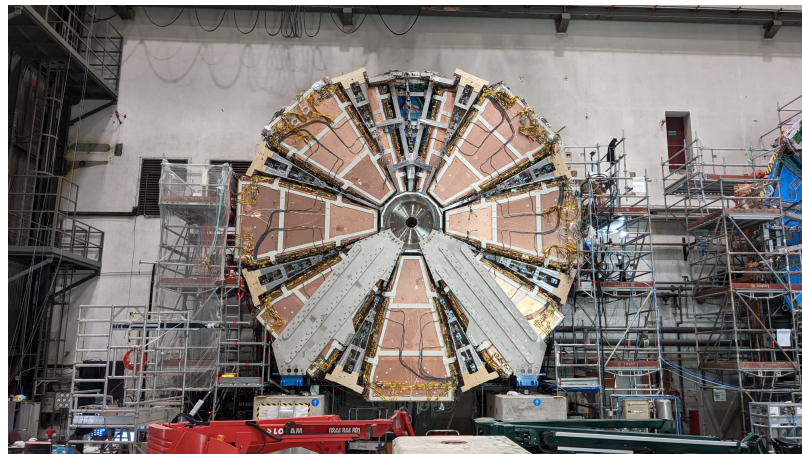
476 of the chambers is to allow matching of track segments measured by the NSW with track
 477 segments from the big wheel to discard tracks not originating from the interaction point.
 478 Figure 4.1 illustrates this point: the Run-2 trigger system would have triggered on all three
 479 tracks (A, B, C) while with the NSW the trigger system would only trigger on track A.
 480 The NSWs will therefore make it possible to maintain a low muon p_T trigger threshold and
 481 maintain an adequate muon momentum resolution during HL-LHC operations, which will
 482 allow the full exploitation of the physics potential of this research program [5].



(a) A sTGC quadruplet module. The left image highlights the trapezoidal shape of a quadruplet module. The right image shows the corner at the short edge, where the four sTGC layers and each layer's gas inlet are visible. The gas outlets and high voltage cables are located along the long edge near the corner in the back left of the photo. The green printed circuit board along the sides are the adaptor boards where the front end electronics are attached.



(b) Left: A sTGC wedge. The white frame outlines the individual quadruplet modules that have been glued together into a wedge. Right: A completed sector, with two sTGC wedges on the outside and two micromegas wedges on the inside.



(c) A picture of one of the two NSWs. All sectors except one large sector at the top are installed, revealing two of the smaller sectors that are normally hidden under the large sectors and support bars. The NSWs are 9.3 m in diameter.

Figure 4.2: Images showing different stages of NSW construction.

483 **4.2 Design of the NSWs**

484 The NSWs are made with two detector technologies: micromegas and small-strip thin gap
485 chambers. Eight layers of each cover the entire area of the wheel. Micromegas are designed
486 to be the primary precision tracking detectors and sTGCs the primary triggering detectors,
487 but both technologies offer full redundancy by being capable of providing both precision
488 measurements and trigger information. Both types of detectors were designed to achieve
489 spatial resolution better than $\sim 100 \mu\text{m}$ per layer. Four chambers are glued together to create
490 quadruplet modules of each detector type. Quadruplets of different sizes, most shaped as
491 trapezoids, are assembled into wedges. Two sTGC wedges and two micromegas wedges are
492 layered to create sectors (with the sTGC wedges on the outside) [5]. Different stages of the
493 construction process are shown in Figure 4.2. At the time of writing, the assembly of the
494 NSWs has just been completed. The first NSW has been lowered into the ATLAS cavern
495 and is being commissioned and the second will be lowered shortly.

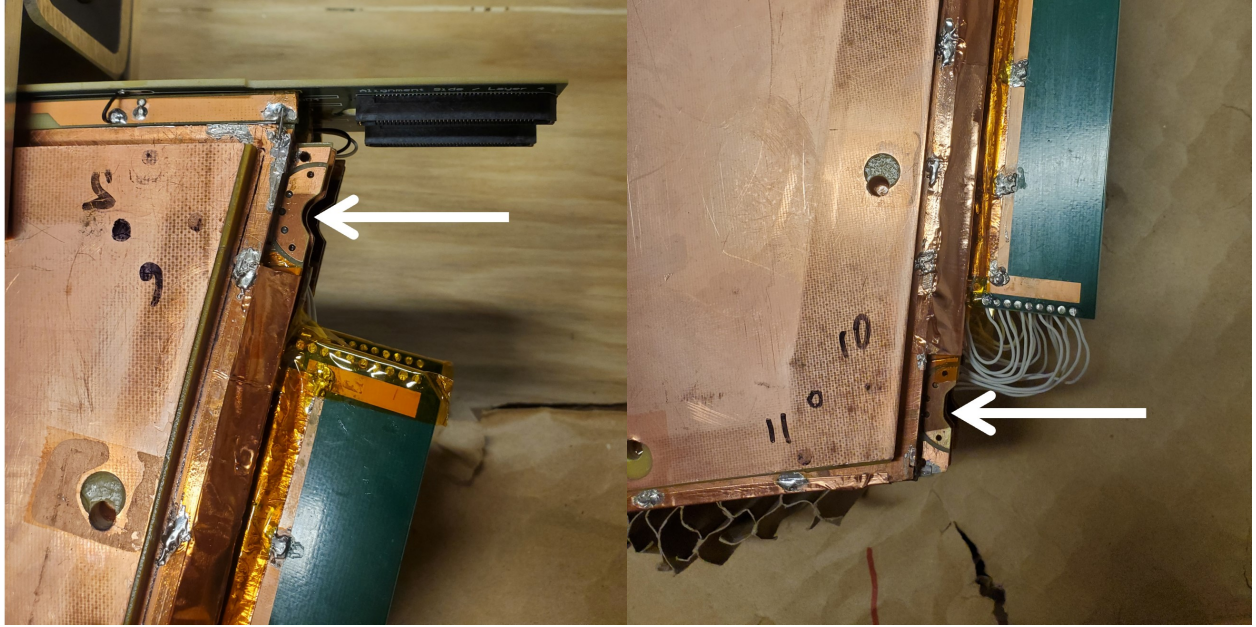
496 **4.3 Small-strip thin gap chambers**

497 The sTGCs are gas ionization chambers operated with a gas mixture of CO₂:n-pentane with
498 a ratio of 55%:45% by volume. Gold-plated tungsten wires, 50 μm in diameter and with
499 1.8 mm pitch, are suspended between two cathode planes made of FR-4, each 1.4 mm away
500 (see Figure 4.3). One cathode board is segmented into copper pads of varying area (with a
501 typical size of $\sim 300 \text{ cm}^2$ each), and the other is segmented into copper strips of 3.2 mm pitch
502 running lengthwise perpendicular to the wires. High voltage is applied to the wires and the
503 cathode planes are grounded [5, 53]. When a muon passes through a sTGC, it will ionize some
504 of the atoms in the gas and the electric field in the gas gap will result in the formation of an
505 ionization avalanche [54]. The motion of the ions and free electrons generates small currents
506 on the nearby wire and capacitatively-coupled strip and pad electrodes [5]. The gas mixture
507 was chosen to absorb excess photons produced in the avalanche that delocalize the avalanche
508 signal [55] and saturate many strip electrodes, preventing the formation of streamers [42].
509 This allows the chambers to be run at a higher high-voltage providing a faster response and
510 higher signal [55]. The resistivity of the carbon coating and capacitance of the pre-preg
511 sheet tune the spread of the charge distribution [56] and the speed of the response [57] to
512 optimize the rate capability. The combined information from the strip readout electrodes
513 and wires provide the location where the muon passed through the chamber. The small pitch
514 of the strip readout electrodes is what allows the quadruplets to deliver good track angular
515 resolution to improve the fake trigger rate and meet the precision tracking requirements [5].



Figure 4.3: Internal structure of an sTGC, zoomed into the area under a pad. High voltage is applied to wires suspended in the gas volume to create an electric field. A passing muon causes an ionization avalanche that is picked up by the wire, strip and pad electrodes [8].

- 516 A 3-out-of-4 coincidence in pad electrodes from each layer of a quadruplet defines a region of
 517 interest where the strip and wire electrodes should be read out. The pad triggering scheme
 518 greatly reduces the number of electrodes that require readout so that a track segment of the
 519 required angular resolution can be provided quickly enough to the hardware trigger [5].
- 520 Signal is read out from groups of successive wires, so the position resolution in the direction
 521 perpendicular to the wires is 10 mm per plane. The wires give the azimuthal coordinate
 522 in ATLAS so the position resolution in this direction is sufficient. Good resolution on the
 523 η coordinate, perpendicular to the strips, is important [5]. In a test beam environment,
 524 the strip spatial resolution of a single sTGC was measured to be 45 microns for muon
 525 perpendicularly incident on the surface of the sTGC. Although the spatial resolution worsens
 526 as function of muon angle measured from normal incidence [58], when four sTGCs are glued
 527 together into a quadruplet the design angular resolution of 1 mrad in the strip coordinate is



(a) Brass insert near long edge.

(b) Brass insert near short edge.

Figure 4.4: The brass inserts sticking out from the gas volumes of an sTGC quadruplet. These inserts were pressed against alignment pins when the individual sTGCs were being glued together.

528 achievable [5, 53].
 529 To achieve the required track angular resolution once installed in ATLAS, the absolute
 530 position of each sTGC strip within the ATLAS coordinate system must be accurately known.
 531 The degree of accuracy required is on the order of the position resolution of the chambers,
 532 $\sim 100 \mu\text{m}$. The NSW alignment system, detailed in Section 4.5, will monitor the position
 533 of alignment platforms installed on the surface of the wedges. The alignment platforms are
 534 installed with respect to an external reference on the sTGCs: two brass inserts on each strip
 535 layer on one of the angled sides of each quadruplet (shown in Figure 4.4). So the challenge
 536 of monitoring the position of the strips in ATLAS was separated into two steps: first, infer
 537 the position of the strips with respect to the brass inserts using the sTGC design geometry;
 538 second, use the alignment system to monitor the position of the alignment platforms. The
 539 next section provides some pertinent details on the sTGC construction process, with steps
 540 that affect the position of the strips with respect to the brass inserts highlighted.

541 4.4 sTGC Quadruplet Construction

542 Five countries were responsible for producing sTGC quadruplets of varying geometries for the
543 NSW: Canada, Chile, China, Israel and Russia. Canada was responsible for the construction
544 of one quarter of the required sTGCs, of three different quadruplet geometries. The steps of
545 the construction process in each country were similar [5]. The process followed in Canada is
546 detailed here.

547 A research group at TRIUMF in Vancouver, British Columbia was responsible for preparing
548 the cathode boards. The boards were made and the electrodes etched on at a commercial
549 laboratory, Triangle Labs, in Carson City, Nevada. Once completed they were sent to TRI-
550 UMF to be sprayed with graphite and to have support structures glued on [7]. The boards
551 are commercial multilayer printed circuit boards, but the strip boards required precision ma-
552 chining to etch the strip pattern [5]. Triangle Labs also machined the two brass inserts into
553 each strip board. A coordinate measuring machine (CMM) was used to accurately measure
554 the position of a set of reference strips on each board. Four quality parameters describing
555 non-conformities in the strip pattern of each board with respect to the brass inserts were
556 derived from the data and the results are available on a QA/QC database. The parameters –
557 offset, angle, scale and nonparallelism – and the CMM data collection is described in full
558 in [7]. Due to time constraints, tolerances on the non-conformities in the etched strip pattern
559 with respect to the brass inserts were loosened, with the condition that the strip positions
560 in ATLAS would have to be corrected for [7].

561 The prepared boards were sent to Carleton University in Ottawa, Ontario for construction
562 into sTGCs and quadruplets. First, the wires were wound around the pad cathode boards
563 using a rotating table and the wires were soldered into place. A wound pad cathode board glued
564 on top to create an sTGC. Holding one sTGC flat with the vacuum, another was glued on
565 top to create a doublet, then two doublets were glued together to create a quadruplet. When
566 gluing sTGCs together, the brass inserts were pushed against alignment pins with the goal of
567 keeping the strip layers aligned within tolerance. However, non-conformities in the shape of
568 the brass inserts, non-conformities in the position of the alignment pins and shifts between
569 sTGCs while the glue cured resulted in misalignments between the brass inserts and strip
570 layers. Precise alignment of the pad boards or wires with respect to the strip boards did
571 not have to be so tightly controlled because pads and wires do not measure the precision
572 coordinate.

574 The Carleton team finished the quadruplets by installing adaptor boards on the angled sides
575 of each layer that allow front end electronics to be attached. Completed quadruplets were sent
576 to McGill University where their performance was characterized with cosmic rays. Details

577 pertaining to cosmic ray testing of sTGC quadruplets at McGill University are described
578 in Chapter 5. Tested quadruplets were sent to CERN where they were assembled into
579 wedges and alignment platforms installed. The alignment platforms were installed using
580 a jig positioned with respect to the brass inserts. Completed wedges were assembled into
581 sectors then installed on the NSWs.

582 The quadruplet construction process had two steps where strip positions could be shifted off
583 of nominal. At board-level, there could be non-conformities in the etched strip pattern with
584 respect to the brass inserts, described by the four quality parameters [7]. At the quadruplet
585 level, misalignments between the brass inserts and strips on different layers were possibly
586 introduced during the gluing. The result was that the brass inserts were not a reliable
587 reference point and that the strips can be offset from their design position by up to hundreds
588 of micrometers. Offsets in strip positions from nominal in Canadian quadruplets were shown
589 to be random [7], so no one correction would suffice. The offsets must be measured and
590 corrected for in the ATLAS offline software that does the precision tracking. Understanding
591 the work ongoing to make measurements of strip position offsets and correct for them requires
592 understanding the strategy of the NSW alignment system.

593 4.5 NSW alignment

594 The idea of the NSW alignment system is presented in [5], but the details have only been
595 presented internally so far. After the wedges are constructed, alignment platforms are in-
596 stalled on every sTGC quadruplet and optical fibres routed to them, as shown in Figure 4.5.
597 Light from the optical fibres will be monitored in real time by cameras (BCAMs) mounted on
598 the alignment bars of the NSWs. The system will thus record the positions of the alignment
599 platforms in the ATLAS coordinate system and any changes over time.

600 The original alignment scheme was to use the brass inserts as a reference between the align-
601 ment platforms and the individual strips, as shown in the solid arrows in Figure 4.6 – this
602 will no longer work. The position of the alignment platforms will be known thanks to the
603 alignment system, so a different method to get the position of the strips with respect to the
604 alignment platforms is currently in its final stage of development. The technique consists of
605 the measurement of the strip pattern offset at a few areas on the surface of a sTGC quadru-
606 plet using an xray gun mounted on the alignment platforms. The local strip pattern offset
607 with respect to nominal geometry at the location of each alignment platform is obtained
608 by analyzing the xray gun beam profile. As shown in Figure 4.6, this approach essentially
609 bypasses the need to know the position of strips with respect to the brass inserts. The align-
610 ment platforms provide the link to the nominal geometry because the nominal group of strips

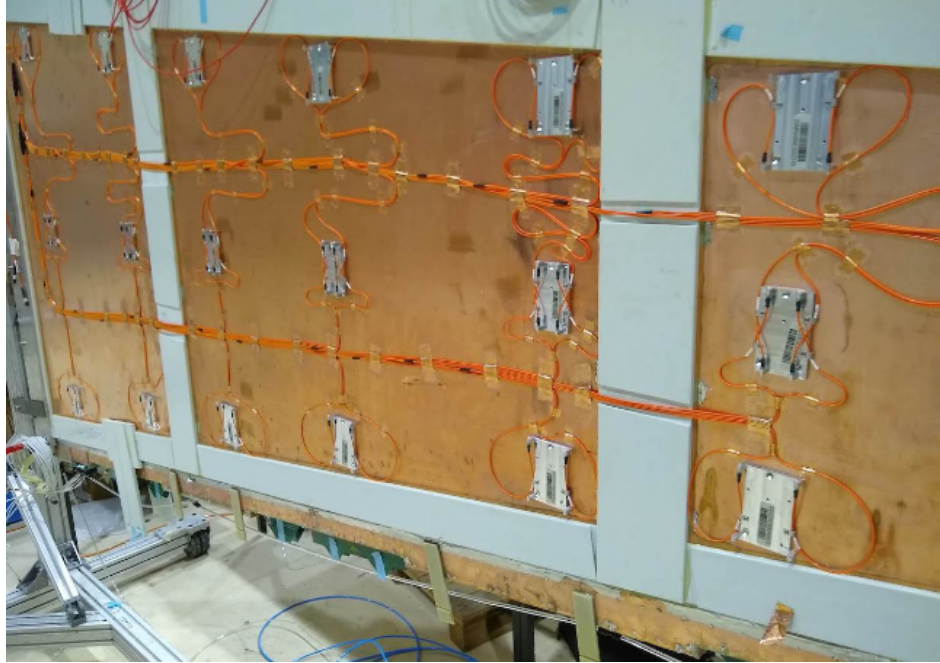


Figure 4.5: A sTGC wedge with alignment platforms (silver) installed on the quadruplet. Optical fibres (orange) are routed to the alignment platforms. Cameras on the frames of the NSWs will record light from the optical fibres to monitor in real-time the position the alignment platforms in the ATLAS coordinate system.

611 that should be nearest to them can be identified using the nominal geometry parameters that
 612 assume the strips are perfectly etched and aligned. Cosmic muon track positions cannot be
 613 compared to the nominal geometry because the alignment platforms are not installed when
 614 cosmics data is collected, so there is no external reference to provide a link to the nominal
 615 geometry.

616 The x-ray method does not have the sensitivity to measure the offset of each strip from
 617 nominal, but what can be measured instead is the offset of the strip pattern in a local area
 618 around the position of the gun. *Local offsets* are used to build an alignment model for each
 619 strip layer. Formally defined, an alignment model is a set of parameters used to estimate the
 620 “as-built” position of a strip given its nominal position. The alignment model currently being
 621 worked on takes x-ray and CMM data as input to calculate an overall offset and rotation of
 622 each strip layer with respect to nominal [8]. The alignment parameters could be described
 623 as “global”, meaning over the whole layer instead of local. Without the x-ray dataset, there
 624 would be no input to the alignment model that takes into account inter-layer misalignments
 625 introduced during quadruplet construction.

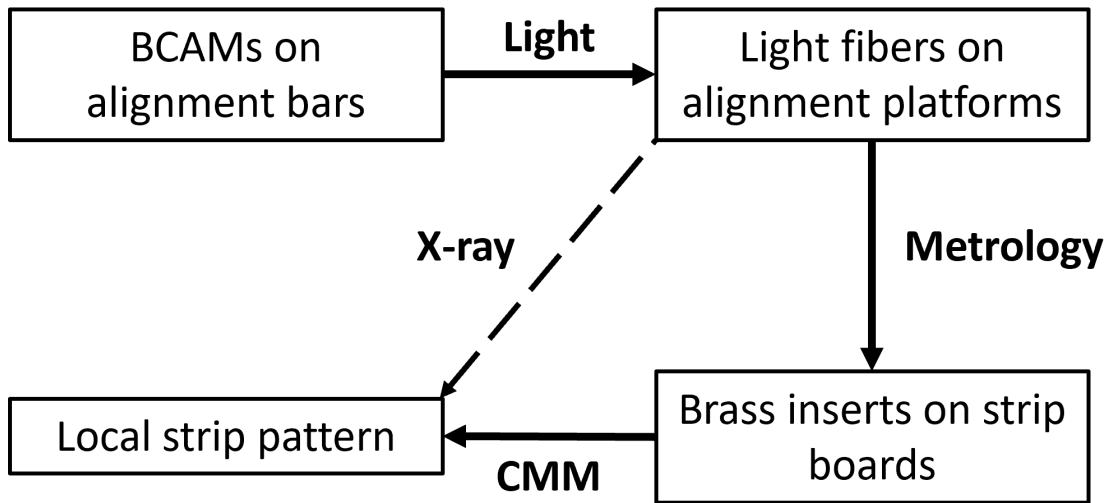


Figure 4.6: Schematic diagram showing how the different elements of the sTGC alignment system relate to one another. The solid arrows denote the planned alignment scheme. The dashed arrow shows the modification being finalized now. This figure was originally designed by Dr. Benoit Lefebvre.

Given that the x-ray local offsets can only be measured at positions where the gun can be attached and that they are an important part of the alignment scheme, the new x-ray measurement technique needs to be validated. The goal of this thesis is to validate the x-ray local offsets while exploring how cosmics data complements and adds to the understanding of strip positions and global alignment.

⁶³¹ Chapter 5

⁶³² Using cosmic muons to measure ⁶³³ relative strip position offsets

⁶³⁴ At McGill University, among other quality and functionality tests, each Canadian-made
⁶³⁵ quadruplet was characterized with cosmic muons. In this chapter, the experimental setup and
⁶³⁶ how the data was analyzed to provide relative strip position offsets is presented. The analysis
⁶³⁷ method was motivated by the how the measurements could be compared to measurements
⁶³⁸ done with the x-ray method (Chapter 6) but also it stands alone as a characterization of the
⁶³⁹ alignment between strips of different layers. The chapter begins with a brief introduction to
⁶⁴⁰ cosmic rays.

⁶⁴¹ 5.1 Cosmic rays

⁶⁴² The earth is being constantly bombarded by particles from the sun, galactic sources and
⁶⁴³ extra galactic sources – collectively called cosmic rays [19, 11]. Cosmic rays consist mostly
⁶⁴⁴ of protons, but also heavier ions, gamma rays and the term sometimes includes neutrinos.
⁶⁴⁵ The primary (initial) cosmic ray interacting with the atmosphere causes electromagnetic and
⁶⁴⁶ hadronic showers of secondary particles. Hadronic showers result from the primary cosmic ray
⁶⁴⁷ interacting strongly with the target of the atmosphere, resulting in an abundant production
⁶⁴⁸ of pions. Charged pions predominantly decay to muons (there is a lesser contribution to
⁶⁴⁹ the muon flux from kaons as well) [59]. The secondary muons are relativistic and thanks
⁶⁵⁰ to time dilation their lifetime is extended as measured in the reference frame of earth, so a
⁶⁵¹ flux of approximately 1 muon/cm²/ min reaches the ground [11]. Measuring the muon flux
⁶⁵² and energy spectrum reveals information about primary cosmic rays [59] which is interesting

653 to high energy physicists and astrophysicists. The muon flux is also terribly convenient for
654 testing muon detectors.

655 **5.2 Experimental setup**



Figure 5.1: Cosmic muon hodoscope at McGill University with a sTGC quadruplet module in the test bench.

656 Cosmic muon characterization of sTGC quadruplet modules was done with a hodoscope, a
657 complete description of which can be found in [58]. The quadruplet was placed in the center
658 of the test bench. Above and below it was a layer of scintillator-PMT arrays, as shown in
659 Figure 5.1. When a cosmic muon passed within the acceptance of the hodoscope, at least one
660 scintillator from the top array and at least one from the bottom array fired in coincidence.
661 A trigger signal was formed using NIM modules from the coincidence of signals from the top

662 and bottom arrays of scintillators. The trigger signal was passed to the front-end electronics
663 attached to the adaptor boards of each layer of the quadruplet.

664 Operating the chambers also required gas and high voltage. A gas mixture of pentane-CO₂
665 in the appropriate proportions was prepared and delivered to each sTGC with a gas system
666 designed and made at McGill University [60]. Since pentane is flammable, the gas system
667 was designed with safety top of mind. The gas system was controlled by a slow control
668 program, also custom made [60]. To prepare the quadruplets for operation, CO₂ was flushed
669 through them overnight to remove potential impurities within each chamber's gas volume.
670 Then, the equivalent of approximately five sTGC gas volumes of the pentane-CO₂ mixture
671 was flushed through to ensure a uniform gas mixture inside the sTGCs; the procedure takes
672 approximately four hours. High voltage was provided by commercial CAEN high voltage
673 boards [60].

674 5.3 Data acquisition

675 Each sTGC electrode was connected to a channel on a prototype ASIC¹ on the front-end elec-
676 tronics, attached to the adaptor boards on each layer of a quadruplet. Each ASIC features
677 64 charge amplifiers with selectable gain and input signal polarities, which output the digi-
678 tized amplitude of the signal at peak for channels above a pre-defined threshold. Thresholds
679 were estimated [62] by optimizing the efficiency of detecting muons while minimizing noise,
680 and further manually tuned in the configuration/readout software before the start of data
681 acquisition for each quadruplet. The signal from the capacitively-coupled strip electrodes
682 has positive polarity and is read out with a gain of one. For each trigger, the signal peak
683 amplitude of all channels above threshold was recorded as an event and stored in a binary
684 file. The readout of strips made use of a special feature of the custom ASIC, the so-called
685 “neighbour triggering” function where signals on channels adjacent to those above threshold
686 are also read out.

687 The quadruplets were held at 3.1 kV for approximately two hours to collect data from
688 approximately 1 million muon triggers.

¹A custom Application Specific Integrated Circuit (ASIC) named VMM3 [61], designed for the readout of signals from the micromegas and sTGCs of the NSWs.

689 **5.4 Data preparation**

690 **5.4.1 Data quality cuts on electrode hits**

691 Corrupted data, if any, is removed while the raw data is being recorded in a binary file. After
692 data taking is completed, the raw data is decoded and the electronics channels are mapped
693 to physical readout electrodes of the quadruplet. The result of this data preparation step is
694 stored in a ROOT [63] tree data format.

695 A hit is defined as a signal recorded from a channel that was above threshold or (in the
696 case of strips) neighbour triggered. In addition to hits from muons, the quadruplets record
697 noise from the electronics and δ -rays (electrons liberated with sufficient energy to escape
698 a significant distance away from the primary radiation and produce further ionization).
699 Therefore, selection cuts are applied to reduce the number of hits that do not originate from
700 muons. Readout strips located at the very edge of the cathode board tend to have higher
701 electronic noise. As a result, all strip hits on a layer where a hit is present on the strips
702 at either edge of the quadruplet are removed from the analysis. A default pedestal value
703 is subtracted from the recorded signal peak amplitude of each electrode for a more realistic
704 estimate of the signal amplitude. Also, events that only have hits on pad electrodes (no
705 strips or wires) were removed from the analysis since these hits are likely from electronic
706 noise, which is higher on the pad readout channels due to their large area.

707 **5.4.2 Clustering and tracking**

708 For events passing the quality selection cuts defined in Section 5.4.1, the x - and y -coordinates
709 of the ionization avalanche on each layer are extracted from the signal on the wires and strips
710 respectively for each event, as shown schematically in Figure 5.2. In this work, x is defined
711 as the coordinate perpendicular to the wires and y is defined as the coordinate perpendicular
712 to the strips. The z -coordinate is perpendicular to the sTGC surface.

713 The x -coordinate of the muon position is taken as the center of the wire group with the
714 maximum peak signal amplitude, since the wire groups' pitch (36 mm) is larger than the
715 typical extent of the ionization charge generated inside a sTGC. Assuming that the true x -
716 position of the hit is sampled from a uniform distribution over the width of the wire group,
717 the uncertainty in the x -position is approximately $\frac{36}{\sqrt{12}}$ mm = 10 mm [64].

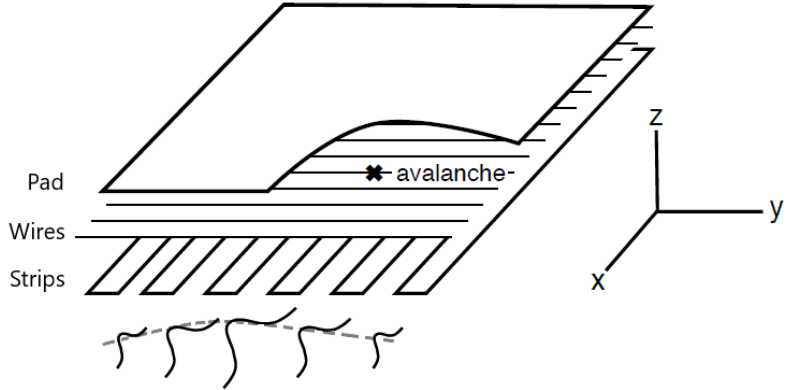


Figure 5.2: Schematic diagram representing the three types of electrodes in a sTGC detector. The position of the ionization avalanche is extracted from the wires and strips that picked up the avalanche signal. The signals on individual strips are sketched. Clustering is the process by which a Gaussian function (represented by the grey dashed line) is fitted to the distribution of the signal amplitude on individual contiguous strips; a sample cluster is shown in Figure 5.3. In this work, the $x(y)$ -coordinate will always refer to the coordinate perpendicular to the wires (strips). The z -coordinate is perpendicular to the sTGC surface [58, 56].

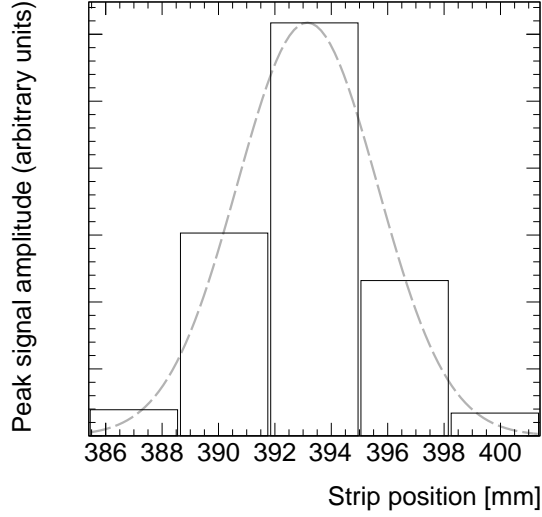


Figure 5.3: A sample cluster resulting from signal recorded on a group of contiguous strips after the passing of a muon. The grey dashed line represents the result of a fit to a Gaussian distribution.

718 The y -coordinate of the muon's position is taken as the Gaussian mean of the peak signal
719 amplitude distribution across a group of contiguous strips that registered hits. The process
720 of grouping contiguous strip hits on a layer is called clustering, and the resulting group is
721 called a cluster. Figure 5.2 sketches the clustering process and a sample cluster is shown
722 in Figure 5.3. The data acquisition system recorded the identification number of the strip
723 electrode that was hit and in the clustering process the position of the center of the strip
724 electrode is calculated based on the nominal quadruplet geometry. Typically, clusters are
725 built of 3-5 strips. The thickness of the graphite coating over the cathode boards determined
726 how many strips picked up the ionization image charge. Larger clusters can often originate
727 from δ -rays since they spread the ionization charge over a larger area.

728 Events are removed from further analysis if there are two reconstructed clusters on one sTGC,
729 since some hits could be from electronic noise or a simultaneous second muon traversing the
730 chamber. Clusters are rejected if the cluster size is lesser than three strips (which should
731 not happen for real events thanks to neighbour triggering), and if the cluster size is greater
732 than 25. After all quality selection cuts are applied on hits and clusters, approximately half
733 of the events recorded remain.

734 The uncertainty on the reconstructed cluster position is assessed by comparing the difference
735 between Gaussian means obtained using two different algorithms. As shown in Appendix A,
736 the difference between the means from the two algorithms considered is found to be ap-
737 proximately 60 μm on average, larger than the statistical uncertainty on the Gaussian mean
738 obtained from the cluster fit. Therefore, an uncertainty of 60 μm is assigned to the recon-
739 structed y -coordinate of a muon.

740 The reconstructed x and y coordinates on each quadruplet layer are used to reconstruct
741 a straight track, independently, in the x - z and y - z planes. Tracks are reconstructed using
742 muon coordinates for every possible pair of two sTGC layers. For example, if an event has
743 muon coordinates reconstructed on all four layers, a total of six track segments in the x - z
744 plane and six track segments in the y - z plane will be reconstructed.

745 5.5 Relative local offsets

746 The offset of a strip from its nominal position can be modeled as a passive transformation.
747 The *local offset* is defined as the shift in the strip pattern with respect to nominal geometry
748 in a specific area of the sTGC. Local offsets systematically change the set of strips nearest
749 to muons passing through an area. The data preparation software assumes that strips are
750 in their nominal positions, so the recorded y -coordinate of the muon on layer i , y_i , is shifted

751 opposite to the layer's local offset, $d_{local,i}$, by

$$y_i = y_{nom,i} - d_{local,i}, \quad (5.1)$$

752 where $y_{nom,i}$ is the position of the muon that would have been recorded on layer i if there
753 was no local offset. Equation 5.1 ignores other factors that affect the cluster position, like
754 position resolution. With cosmics data, there was no external reference to measure $y_{nom,i}$
755 and the local offset is unknown. Therefore, only *relative* local offsets can be measured.

756 To measure relative local offsets, two of the four sTGC layers are chosen to provide a reference
757 coordinate system. Relative local offsets are calculated with respect to the two reference
758 or fixed layers. The hits on the two fixed layers were used to create tracks that can be
759 interpolated or extrapolated (polated) to the other two layers. The set of two fixed layers
760 and the layer polated to are referred to as a tracking combination. The residual of track i ,
761 Δ_i , is defined as,

$$\Delta_i = y_i - y_{track,i}, \quad (5.2)$$

762 where $y_{track,i}$ is the polated track position on the sTGC layer the residual is measured on.
763 Track residuals are affected by the local offset in the area of each layer's hit. As an example,
764 in Figure 5.4, the residual on layer 2 perhaps indicates that layer 2 is offset with respect
765 to layers 1 and 4 in the area of the track. Of course, a single track residual says nothing
766 of the real relative local offset because of the limited spatial resolution of the detectors and
767 fake tracks caused by noise or delta rays. However, the mean of residuals for all tracks in a
768 region of interest will be shifted systematically by the local offsets between layers [58]. For
769 a quadruplet with nominal geometry, the mean of residuals should be zero in all regions and
770 for all reference frames, unlike the example regions in Figure 5.5. The value of the mean of
771 residuals is a measure of the relative local offset of the layer with respect to the two fixed
772 layers used to reconstruct the muon track. The sign convention is such that the mean of
773 residuals is opposite to the relative local offset.

774 To study the relative local offsets, residual distributions across each strip layer of a quadruplet
775 for all possible tracking combinations are assembled and fitted. As expected, the residual
776 distributions are wider for tracking combinations where the extrapolation lever arm is largest,
777 as in the example distributions shown in Figure 5.5. In general, residual means from dis-
778 tributions of residuals with geometrically less favourable tracking combinations have larger
779 statistical and systematic uncertainties. The bin size of 200 μm for the distributions shown
780 in Figure 5.5 was chosen based on the uncertainty on residuals calculated from tracks on
781 layer 4 (1) built from hits on layers 1 and 2 (3 and 4) given a cluster y -coordinate uncertainty
782 of 60 μm (discussed in Section 5.4.2 and Appendix A), since these tracks yield residuals with
783 the largest uncertainties.

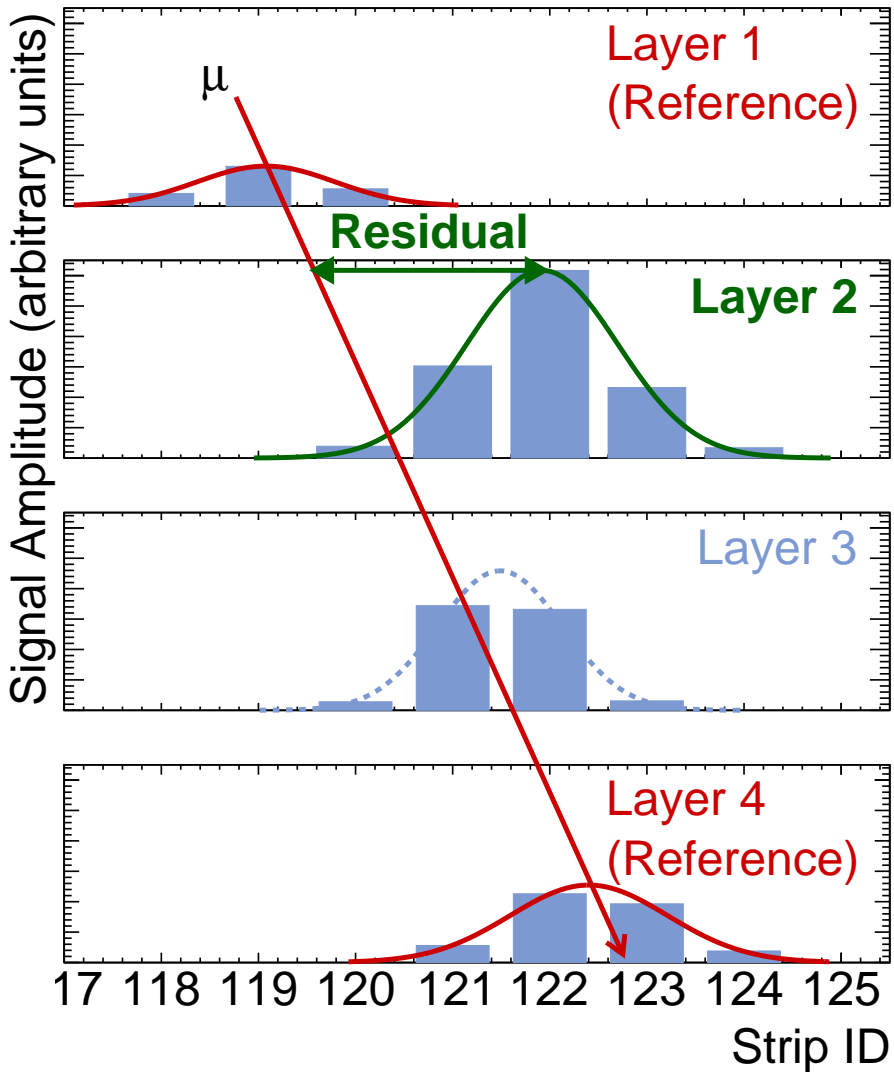
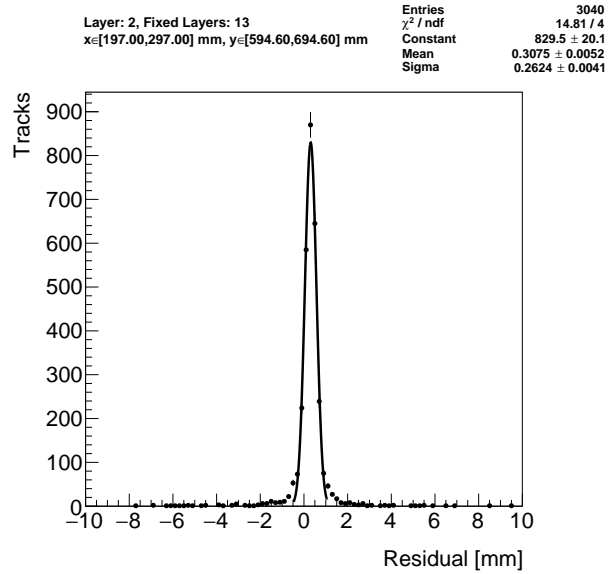
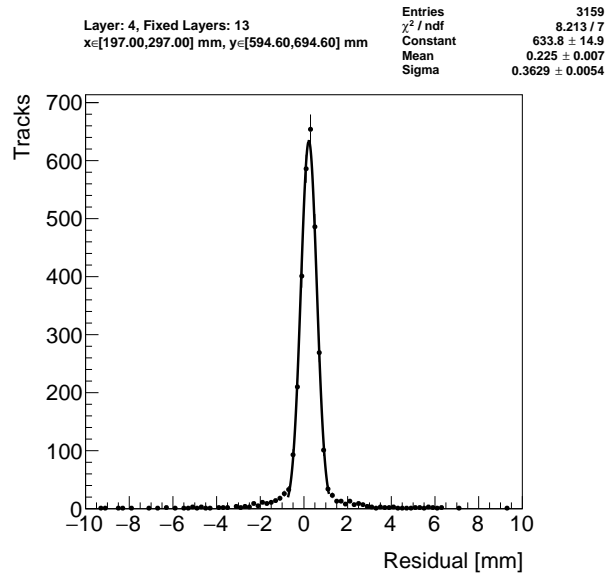


Figure 5.4: Representation of a muon event recorded by an sTGC quadruplet. The charge clusters measured using strip electrodes are fit with a Gaussian distribution and the fitted mean is taken as the reconstructed muon position. A track is built from the chosen reference layers, 1 and 4, and the track residual is calculated on layer 2. The clusters come from a real muon, but their positions were modified to highlight the non-zero value of the residual on layer 2.



(a) Tracks on layer 2, reference layers 1 and 3.



(b) Tracks on layer 4, reference layers 1 and 3.

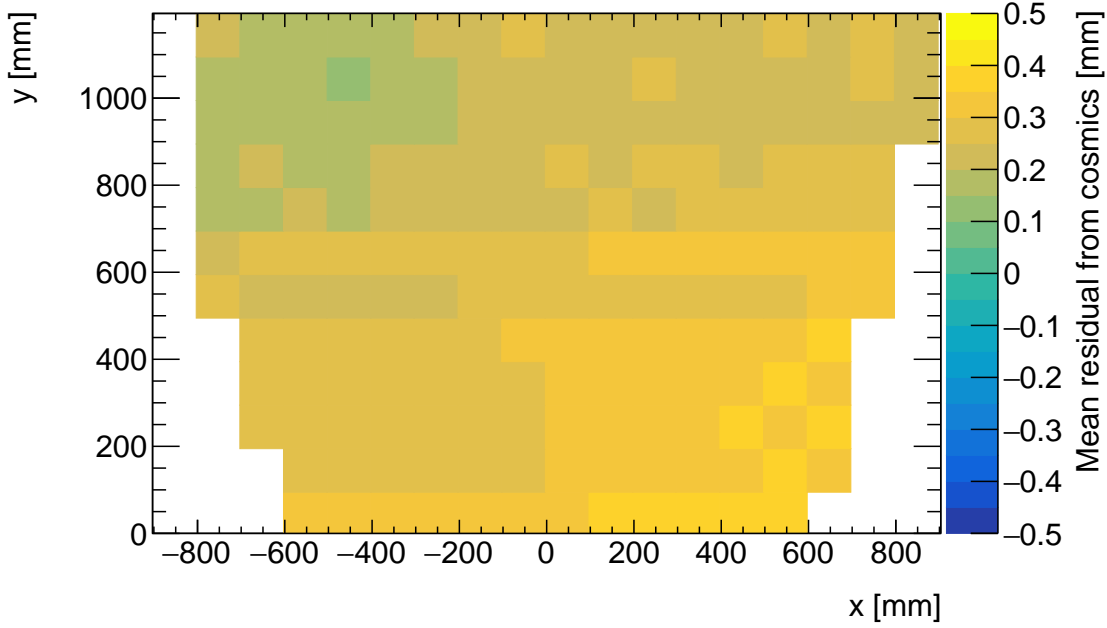
Figure 5.5: Residual distribution in the region $x \in [197, 297]$ mm, $y \in [594.6, 694.6]$ mm (100 mm by 100 mm area) for two different tracking combinations. Data from quadruplet QL2.P.11.

784 A Gaussian fit is used to extract the mean of the residual distributions. The residual distri-
785 butions are actually better modeled by a double Gaussian distribution, which better captures
786 the distribution tails in Figure 5.5. However, a study described in Appendix C.1 found that
787 a fit to a single Gaussian function in the core of the distribution is sufficient to reconstruct
788 the mean of the distribution.

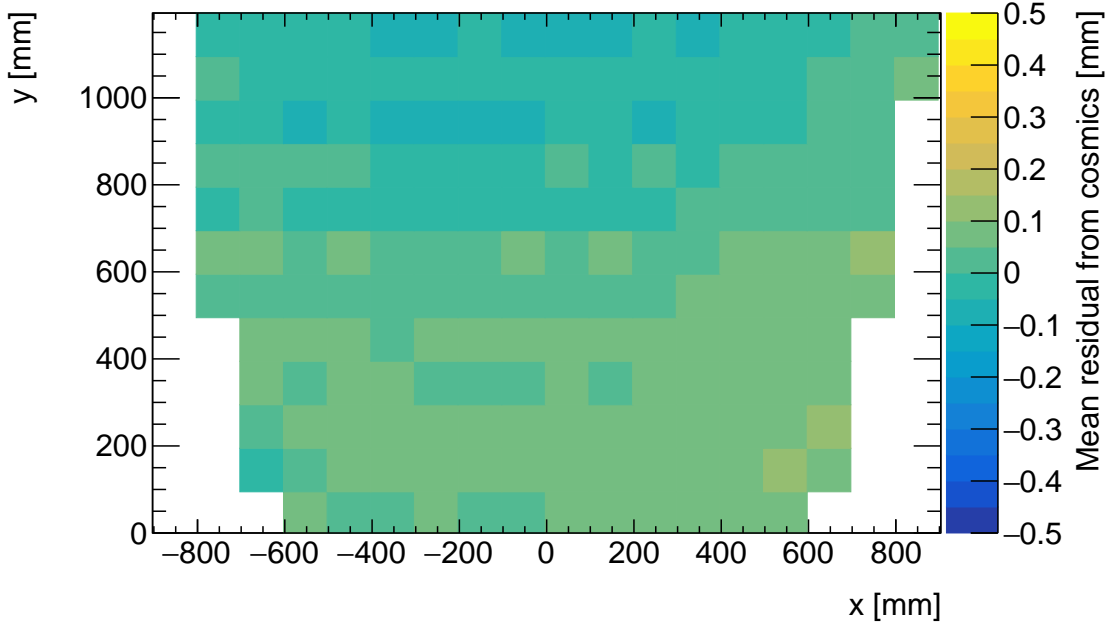
789 The area of the region of interest where tracks residuals were included in the residual distri-
790 bution was 100 mm by 100 mm. The size balanced the number of tracks falling in the region
791 of interest to give a small statistical uncertainty on the fitted mean while being smaller
792 than the order on which local offsets were expected to change significantly. “Significantly”
793 was defined as 100 μm , the required position resolution of the sTGCs and the precision to
794 which strip positions should be known. The distance over which local offsets are expected to
795 change significantly can be estimated using a simple alignment model. Assuming the strips
796 of a layer have been displaced uniformly from their nominal positions by a global offset and
797 rotation, the distance in x that a large but possible rotation of 1 mrad changes the local
798 offset by 100 μm is 100 mm.

799 The means of residuals are plotted across each sTGC layer for every possible tracking combi-
800 nation to get a picture of the how the relative local offsets change as a function of position
801 over the layer’s surface. Figure 5.6 shows the mean of residuals on layer 2 calculated with
802 layers 1 and 3 as reference for two different quadruplets, referred to as QL2.P.11 and QL2.P.8.
803 In Figure 5.6a, the Gaussian mean of the residual distribution in Figure 5.5a is the entry in
804 the bin defined by the boundaries $x \in [197, 297]$ mm, $y \in [594.6, 694.6]$ mm.

805 Many of the residual means are non-zero and change smoothly over layer 2, indicating that
806 there are relative local offsets stemming from global misalignments between the strip patterns
807 of different sTGC layers in both quadruplets. Given that the residual mean changes with x
808 in Figure 5.6a, quadruplet QL2.P.11 likely has a rotation of layer 2 with respect to layers
809 1 and 3, combined with an offset of the entire layer. The residual means are smaller in
810 Figure 5.6b indicating that quadruplet QL2.P.8 is less misaligned overall than QL2.P.11;
811 however, the relative local offsets range between $\pm 200 \mu\text{m}$ so they are significant enough to
812 warrant a correction so the quadruplet can achieve the required track angular resolution in
813 the NSW.



(a) Mean of track residuals on layer 2, obtained using layers 1 and 3 as reference, for QL2.P.11.



(b) Mean of track residuals on layer 2, obtained using layers 1 and 3 as reference, for QL2.P.8.

Figure 5.6: Mean of residuals in each 100 mm by 100 mm bin over the area of sTGC layer 2 for quadruplets QL2.P.11 and QL2.P.8. The entry in $x \in [197, 297]$ mm, $y \in [594.6, 694.6]$ mm of Figure 5.6a corresponds to the fitted Gaussian mean in Figures 5.5a. The mean of residuals has the same value and opposite sign to the relative local offset of layer 2 with respect to the reference frame defined by layers 1 and 3.

814 **5.6 Systematic uncertainty**

815 The statistical uncertainty on the local residual means was typically around 10 - 20 μm , and
816 Appendix B shows that the analysis is not statistically limited by the number of triggers
817 collected for each quadruplet. Systematic uncertainties were found to be larger than the
818 statistical uncertainty on the residual means.

819 Several analysis choices had some degree of impact on the fitted means of local track residual
820 distributions. To study the impacts, the residual means were calculated in different ways and
821 distributions of the differences made. The complete studies are shown in Appendix C. The
822 root-mean-square (RMS) of the residual mean difference distributions were used to quantify
823 the impact of the different analysis choices as systematic uncertainties on the residual means.
824 The following analysis choices are considered:

- 825 • The impact of performing a single or double Gaussian fit on the track residual dis-
826 tributions is studied. As shown in Appendix C.1, the difference between fitting the
827 track residual distribution with a single or double Gaussian function varies between
828 10-30 μm from the most to least geometrically favourable tracking combinations.
- 829 • The impact of the operating voltage used during data taking is investigated. Cosmic
830 muon data was recorded at 2.9 kV and 3.1 kV. As described in Appendix C.2, an
831 uncertainty between 10-40 μm is assigned to the different tracking combinations.
- 832 • The impact of using different Gaussian fitting algorithms used to reconstruct the po-
833 sition of a charge cluster was considered. Clusters are fit with the Minuit2 [65] and
834 Guo's method [66]. As shown in Appendix C.3, the resulting difference in residual
835 means is between 10-30 μm from the most to least geometrically favourable tracking
836 combinations.
- 837 • The impact of correcting reconstructed cluster positions for differential non-linearity
838 (DNL) is studied. DNL is fully described in Appendix C.4. It is a bias in the recon-
839 structed cluster position that comes from discretely sampling a continuous distribu-
840 tion, in this case the charge distribution [67, 58, 6]. The difference between residual
841 means is compared with and without correcting the reconstructed cluster positions.
842 Appendix C.4 shows that the impact of the correction is smaller than 10 μm for all
843 tracking combinations, which is almost negligible.

844 A summary of the systematic uncertainties assigned to the local means of residuals for each
845 tracking combination is given in Table 5.1. The RMS of the distributions of residual mean
846 differences of geometrically similar tracking combinations are averaged and the average value

Tracking geometry	Residual distribution fit function (C.1)	Cosmics data collection voltage (C.2)	Cluster fit algorithm (C.3)	Apply DNL correction or not (C.4)	Total
Similar to layer 3, fixed layers 1, 2	0.01 mm	0.04 mm	0.02 mm	0.01 mm	0.05 mm
Similar to layer 4, fixed layers 1, 2	0.03 mm	0.01 mm	0.03 mm	0.01 mm	0.10 mm
Similar to layer 2, fixed layers 1, 3	0.01 mm	0.02 mm	0.01 mm	0.000 mm	0.03 mm
Similar to layer 4, fixed layers 1, 3	0.01 mm	0.04 mm	0.01 mm	0.01 mm	0.04 mm
Similar to layer 2, fixed layers 1, 4	0.01 mm	0.04 mm	0.01 mm	0.01 mm	0.04 mm

Table 5.1: Systematic uncertainties assigned for each analysis option per tracking combination. Details can be found in Appendix C. The total systematic uncertainty is obtained by summing in quadrature all the individual systematic uncertainties.

847 is taken as the systematic uncertainty for those tracking combinations. An example of a ge-
 848 ometrically similar pair of tracking combinations is fixing layers 1 and 2 and extrapolating
 849 to layer 3 or fixing layers 2 and 3 and extrapolating to layer 4; geometrically similar combi-
 850 nations have the same polation lever arm. The total systematic uncertainty is obtained by
 851 summing in quadrature all the different sources of systematic uncertainty. The uncertainty
 852 in each mean of residuals is obtained by summing in quadrature the statistical uncertainty
 853 in the mean of residuals and the appropriate systematic uncertainty for the tracking com-
 854 bination used to calculate the mean of residuals.

855 **5.7 Discussion**

856 The total uncertainty in the residual means, and hence the relative local offsets, is typically
857 less than the design sTGC position resolution of $\sim 100 \mu\text{m}$ [5]. Therefore, the residual means
858 are relevant input for alignment studies.

859 The relative local offsets calculated from the means of residual distributions over the surface
860 of an sTGC layer for all tracking combinations provide a complete picture of the relative
861 alignment between sTGC layers in a quadruplet module. In fact, cosmic muon testing is the
862 only characterization technique where the entire surface of quadruplet layers can be probed
863 since muons hits are distributed almost uniformly; the CMM [7] and x-ray methods [8] depend
864 on measurements at reference points, and test beams only have a limited beam spot to work
865 with [6]. By looking at 2D-histograms of residual means like Figure 5.6 for all tracking
866 combinations, it is easy to identify quadruplets that suffer large relative misalignment since
867 many residual means differ significantly from zero. Moreover, the pattern in the residual
868 means can be used to motivate a physical interpretation of misalignments. The residual
869 means can be used as a reference, cross check, or input to other alignment studies.

870 Relative local offsets cannot be used to position strips in the absolute ATLAS coordinate
871 system because there is no external reference to measure positions on all layers with respect
872 to. The lack of an external absolute reference frame means that there is not enough infor-
873 mation to unfold relative local offsets into absolute local offsets (with respect to the nominal
874 quadruplet geometry). As an example, assuming that the residual on layer 2 in Figure 5.4 is
875 representative of the absolute value of the relative local offset, the residual on layer 2 could
876 be caused by the strips on layer 2 being misaligned from nominal, but it could also be caused
877 by strips on layers 1 and 4 being offset from nominal while the strips on layer 2 are in their
878 nominal positions! Any number of combinations of local offsets on layers 1, 2 and 4 could
879 produce the residual on layer 2. Absolute local offsets must be calculated using another
880 method: the x-ray method.

881 **Chapter 6**

882 **Using x-rays to measure relative strip
883 position offsets**

884 This chapter describes the analysis of x-ray data to measure relative local strip position
885 offsets, which can be compared with results obtained using cosmic data. The reader is re-
886 ferred to the paper describing the x-ray method [8]. Some minor changes to the experimental
887 setup have been made since the paper was written. The experimental setup described here
888 is current and was used to collect the data presented in this thesis.

889 **6.1 Experimental setup**

890 The x-ray tests were performed after the quadruplets had arrived at CERN, had been were
891 assembled into wedges, and the alignment platforms installed. An x-ray gun was attached to
892 one of the alignment platforms glued to the surface of the wedge and the x-ray beam profile
893 was recorded by the strip electrodes.

894 The sTGC wedges were installed on carts that could rotate their surface to a horizontal
895 position. A mounting platform was installed on top of the alignment platform using a three-
896 ball mount. The x-ray gun used was an Amptek Mini-X tube [68]. The x-ray gun was placed
897 in a brass holder with built-in 2 mm collimator and 280 μm copper filter. The holder was
898 mounted on one of five positions on the mounting platform, as shown in Figure 6.1. The
899 x-ray gun positions were chosen to avoid wire support structures in the sTGCs that reduce
900 hit efficiency [58] and boundaries between sets of strips read out by two different ASICs that
901 could each have different thresholds.

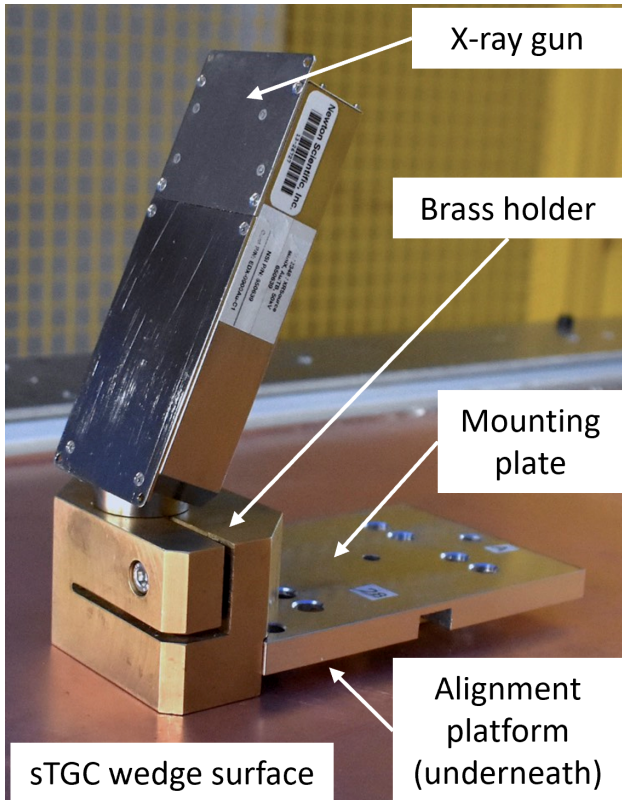


Figure 6.1: The x-ray gun mounted to an alignment platform on the surface of a sTGC wedge. Adapted from [8].

902 As with cosmics data collection, each sTGC also needed gas and high voltage to operate.
 903 Each sTGC layer was operated at 2.925 kV with high voltage from a NIM crate. The sTGC
 904 gas volumes were flushed with CO₂ before and during data collection. The sTGCs were not
 905 operated using the nominal pentane-CO₂ gas mixture due to constraints in its availability
 906 based on safety concerns. The sTGC efficiency is significantly lower when operated with
 907 only CO₂.
 908 The gun produced x-rays with energies under 40 keV with peaks in the 7-15 keV range. Peaks
 909 in the 0-30 keV range were filtered out by the copper filter and the copper of the sTGCs. The
 910 x-rays mostly interacted with the sTGC wedge's copper electrodes and gold-plated tungsten
 911 wires via the photoelectric effect. The resulting photoelectrons that enter the gas volume
 912 caused ionization avalanches which were picked up by the readout strips.

913 **6.2 Data acquisition**

914 A different version of the same front end electronics, but the same ASIC, as used in cosmics
915 testing were used for the x-ray testing to measure the peak signal amplitude. Data was
916 collected for two minutes per gun position with random triggers. A trigger recorded all
917 signals above threshold. Pad and wire data was not recorded.

918 **6.3 Data preparation**

919 Following a similar approach to the cosmics data analysis described in Chapter 5, a default
920 pedestal is subtracted from the signal peak amplitude on each electrode.

921 Clusters are defined as groups of contiguous strip hits recorded within 75 ns. The distribution
922 of peak signal amplitude from continuous strip hits is fitted with a Gaussian function, and the
923 mean of the fitted Gaussian is taken as the cluster position. Cluster positions are corrected
924 for differential non linearity (or DNL, see definition in Appendix C.4). Although the impact
925 of the DNL correction on the reconstructed cluster means is small, it is important to improve
926 the spatial resolution of the sTGC strip layer. Only clusters composed of hits on 3-5 strips
927 are used in the x-ray analysis. Clusters with signal on more than five strips are cut because
928 they were most likely caused by photoelectrons ejected with enough energy to cause more
929 primary ionization and subsequent avalanches as δ -rays.

930 The x-ray analysis diverges entirely from the cosmics analysis algorithm here because the
931 ionization from x-rays does not originate from one charged particle traversing all layers
932 of a sTGC quadruplet, so there is no track to rebuild. Rather, ionization avalanches [54]
933 are generated by photoelectrons liberated from the metals of the sTGCs, which only travel
934 through one gas volume and are produced at all angles. Instead of reconstructing a straight
935 line trajectory through multiple sTGC layers, the cluster position distribution on each sTGC
936 layer is used to reconstruct the beam profile. A typical x-ray beam profile is shown in
937 Figure 6.2.

938 **6.4 Measuring local offsets**

939 The fitted Gaussian mean of the cluster position distribution is taken as the reconstructed
940 center of the x-ray beam profile on each sTGC layer. The reconstructed center is compared to
941 the expected beam profile center, calculated in two steps. First, the position of the alignment
942 platform with respect to the brass inserts and the nominal position of the strips under the

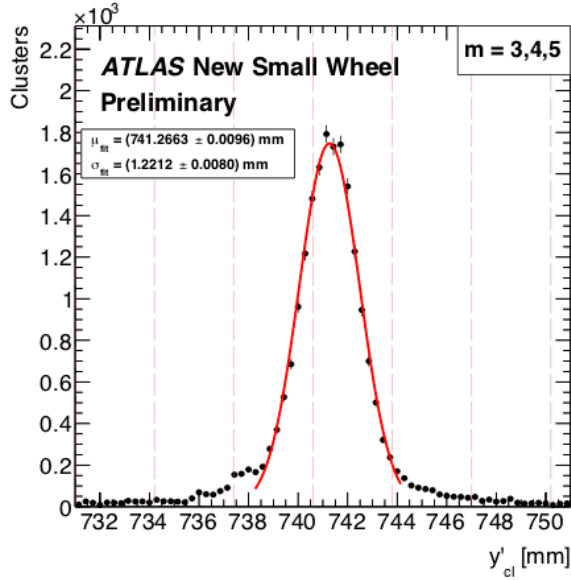


Figure 6.2: An example distribution of x-ray cluster mean positions after the analysis selection cuts and DNL corrections are applied. The strip cluster multiplicity, m , was limited to 3, 4 or 5. The red curve is a Gaussian fit of the distribution and the pink dashed lines denote the edges of the strips [8].

943 gun position with respect to the brass inserts are used to calculate the expected beam profile
 944 center assuming a nominal quadruplet geometry. Second, the expected beam profile center
 945 is corrected for the geometry of the brass holder, the positioning and angle of the alignment
 946 platforms, and the beam angle. The difference between the expected and reconstructed beam
 947 profile centers is a measure of the local offset of the strip electrode pattern. Applying the
 948 logic of Equation 5.1 to the beam profile, the Gaussian mean of cluster positions on the given
 949 layer acts as the recorded position, y_i , the expected center is $y_{nom,i}$ and the local offset is
 950 $d_{local,i}$ as before, where i denotes the layer. Since the position of the alignment platforms will
 951 be monitored continuously by the alignment system in ATLAS [5], the position of the strips
 952 that should have been at the x-ray gun position are shifted by $d_{local,i}$ and so their absolute
 953 positions in the ATLAS coordinate system are known for every position where x-ray data
 954 was recorded. Therefore, the x-ray local offsets can be used to measure the position of
 955 some strips in the ATLAS coordinate system, as is required for the triggering and precision
 956 tracking goals of the NSWs as discussed in Chapter 4.

957 Studies of systematic effects on the measured beam profile centers lead the x-ray working
 958 group to accept an uncertainty of 120 μm on the beam profile centers. The largest uncertainty

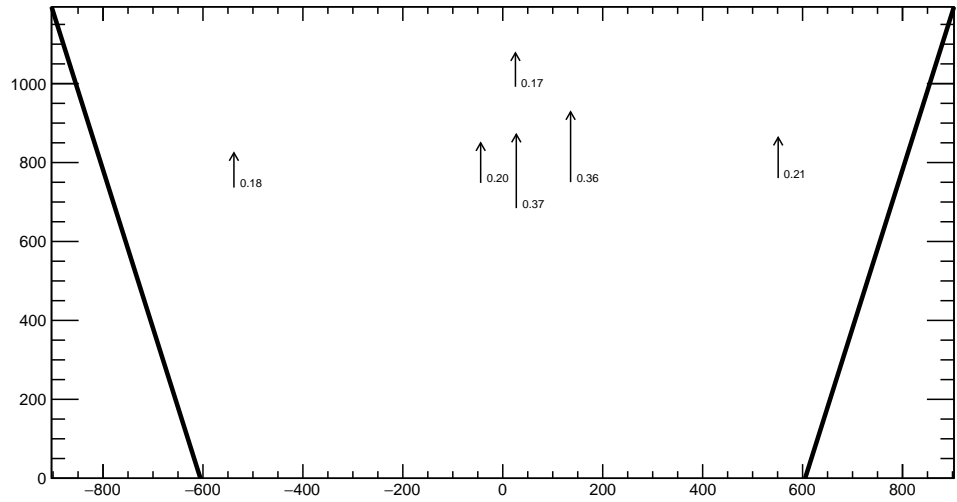
959 comes from the effect of the gun angle, which proved difficult to measure and correct for.
960 The details and results of the systematics studies have not been published externally.

961 The absolute local strip offsets measured using the method described above are not presented
962 here as the author did not conduct this work. However, the author used the *absolute* local
963 offsets to calculate *relative* local offsets that can be compared to the relative local offsets
964 measured using cosmic muon data.

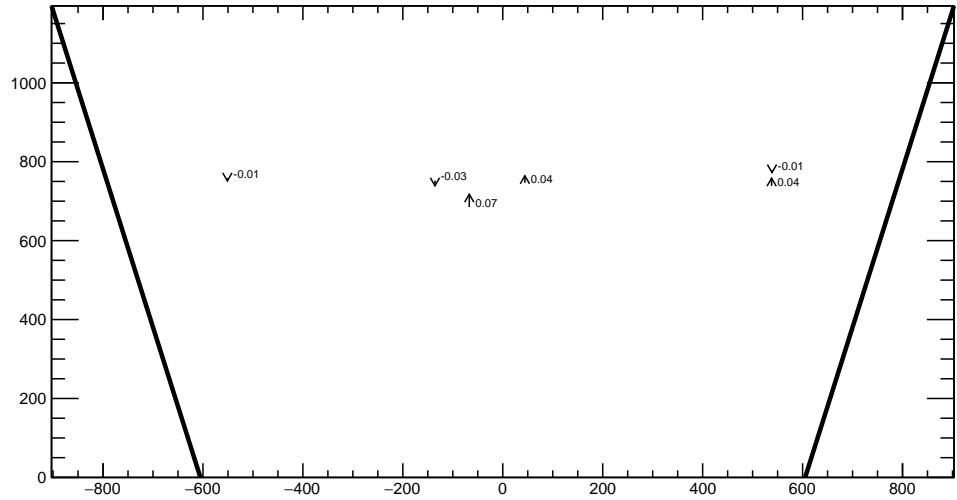
965 6.5 Measuring relative local offsets

966 The novelty of the x-ray method and the uncertainty in the x-ray local strip position offsets,
967 which greater than the precision to within which the position of the strips would ideally be
968 known, means that the x-ray local offsets should be validated by an independent method.
969 Absolute local offsets measured using x-ray data and relative local offsets measured using
970 cosmics data cannot be compared directly because they are not defined with respect to the
971 same coordinate system: x-ray absolute local offsets are measured in the ATLAS coordinate
972 system while cosmics relative local offsets are defined with respect to a reference frame
973 established by two sTGC layers in a quadruplet. The following describes the method used to
974 calculate relative local strip position offsets from the x-ray local offsets that can be compared
975 to the cosmics relative strip position offsets.

976 Given that the measured x-ray beam profile centers are systematically affected by local strip
977 position offsets in the same way as the means of the cosmic ray track residual distributions,
978 the x-ray beam profile centers on each sTGC layer are used to reconstruct a straight line in
979 the y - z plane using the beam profile centers on two sTGC layers chosen as reference, in a
980 manner similar to the track reconstruction performed with cosmic muon data. A residual
981 is calculated as the difference between the beam profile center on the layer of interest and
982 the polated straight line fitted from two sTGC layers taken as a reference. The beam profile
983 center on the layer of interest acts as y_i and the polated track position acts as $y_{track,i}$ in
984 Equation 5.2. As with the means of cosmic track residual distributions, the sign convention
985 is such that the x-ray residual is opposite in sign to the relative local offset of the layer of
986 interest with respect to the two fixed layers.



(a) X-ray residuals on quadruplet QL2.P.11 layer 2 obtained using reference layers 1 and 3.



(b) X-ray residuals on quadruplet QL2.P.8 layer 2 obtained using reference layers 1 and 3.

Figure 6.3: The x-ray residuals on sTGC layer 2 calculated with respect to the beam profile centers on sTGC layers 1 and 3 for quadruplet QL2.P.11 (a) and QL2.P.8 (b). The arrows originate from the expected position of the beam profile center assuming a nominal geometry. The lengths of the arrows are 500 times the value of the x-ray residuals, scaled for visibility. The value of the x-ray residuals are annotated in millimeters and have an uncertainty of ± 0.15 mm.

987 For each x-ray survey position, the x-ray residuals were calculated for all possible pairs of
988 sTGC layers taken as reference and each sTGC layer the straight line could be polated to, as
989 was done for cosmic muon tracks. Calculating a residual required x-ray beam profiles on at
990 least three layers. Figure 6.3 shows the x-ray residual values on sTGC layer 2 with respect to
991 reference layers 1 and 3 for sTGC quadruplet modules QL2.P.11 and QL2.P.8. For module
992 QL2.P.11, a negative relative local offset is measured at all x-ray survey points, indicating a
993 global translation of sTGC layer 2 with respect to layers 1 and 3.
994 The uncertainty on the x-ray residualsis is obtained by propagating the uncertainty on the
995 reconstructed x-ray beam profile centers ($120\text{ }\mu\text{m}$) through the polation. The uncertainty
996 on the x-ray residuals ranges from $150\text{ }\mu\text{m}$ to $400\text{ }\mu\text{m}$ from the most to least geometrically-
997 favourable tracking combination. There is no discernible pattern of misalignmnet revealed by
998 the x-ray residuals on QL2.P.8 because they have absolute values smaller than the uncertainty
999 on the x-ray residuals ($150\text{ }\mu\text{m}$).
1000 The relative local offsets calculated using cosmics data and x-ray data will be compared in
1001 the next chapter.

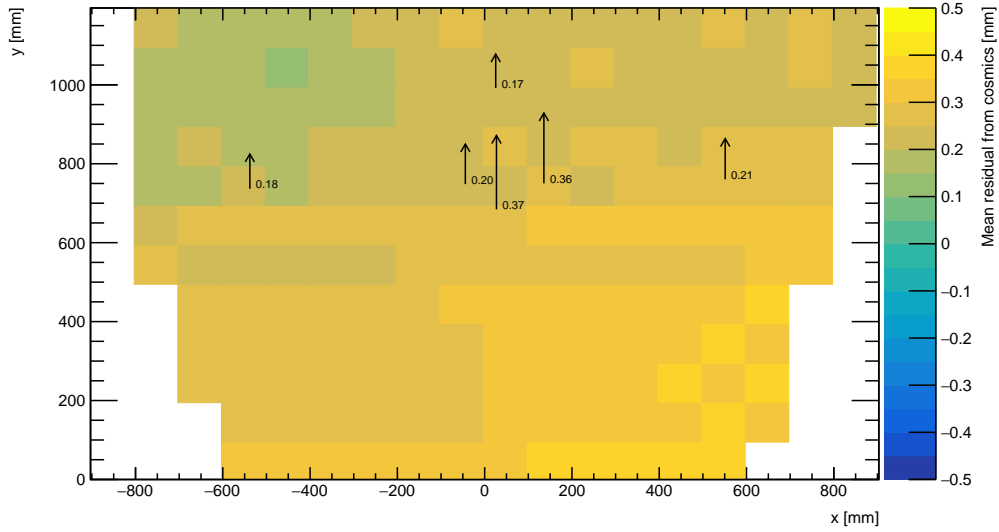
1002 Chapter 7

1003 Comparing cosmic muon and x-ray 1004 relative strip position offsets

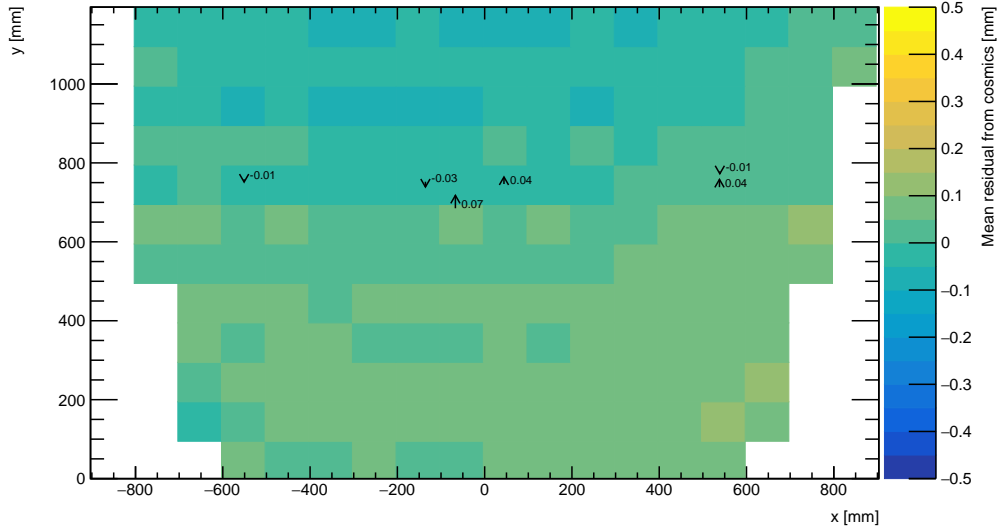
1005 The goal of the work presented in this thesis is to validate the local strip position offsets
1006 measured with x-ray data with results obtained using cosmic ray data. The challenge was
1007 that the x-ray dataset provided absolute local offsets measured in the ATLAS coordinate
1008 system while the cosmics dataset provided relative local offsets measured with respect to a
1009 reference frame defined by two of four sTGC layers in a quadruplet – which could not be
1010 compared directly. To address the challenge, the x-ray local offsets were used to calculate
1011 relative local offsets. Relative local offsets on each sTGC layer obtained with x-ray and
1012 cosmics data calculated using the same two sTGC reference layers are compared for each
1013 area where x-ray data is available. The results of the comparison are presented here.

1014 7.1 Results

1015 Relative local offsets have the same value but opposite sign to the mean cosmics and x-ray
1016 residuals. For the remainder of this chapter, the means of cosmic track residual distributions
1017 will be referred to as mean cosmics residuals.
1018 Mean cosmics and x-ray residuals on sTGC layer 2 calculated with reference layers 1 and 3
1019 across the quadruplet surface are shown in Figure 7.1 for sTGC quadruplets QL2.P.11 and
1020 QL2.P.8. Figure 7.1 is a superposition of Figures 5.6 and 6.3.



(a) Mean cosmics and x-ray residuals on sTGC layer 2 of quadruplet QL2.P.11 obtained using reference layers 1 and 3.



(b) Means cosmics and x-ray residuals on sTGC layer 2 of quadruplet QL2.P.8 obtained using reference layers 1 and 3.

Figure 7.1: The mean cosmics residuals are shown using colour. The x-ray residuals available at nominal gun positions are drawn as arrows and the value of the residual annotated in millimeters with uncertainty ± 0.15 mm. The length of the arrows is 500 times the value of the x-ray residual, scaled for visibility. These plots are a superposition of Figures 5.6 and 6.3.

1021 Figure 7.1a shows that for QL2.P.11 the x-ray residuals are of the same sign and order as
1022 the mean cosmics residuals, as can be seen by comparing the annotated value of the x-ray
1023 residual to the mean cosmics residual represented in the nearest coloured bin. QL2.P.11's
1024 mean cosmics and x-ray residuals are correlated.

1025 For QL2.P.8, Figure 7.1b shows that the x-ray residuals are of the right order compared
1026 to the mean cosmics residuals; however, the value of the x-ray residuals are within their
1027 uncertainty so the correlation is not manifest. While the x-ray residuals do not reveal a
1028 pattern in the relative local offsets across the layer's surface, the mean cosmics residuals
1029 show a structure to the relative local offsets, revealed by how they vary smoothly over the
1030 surface of sTGC layer 2.

1031 The comparison of mean cosmics and x-ray residuals was done for several sTGC quadruplets
1032 for all possible tracking combinations. Scatter plots of the x-ray and mean cosmics residuals
1033 on QL2.P.11 and QL2.P.8 for all tracking combinations are shown in Figures 7.2 and 7.3
1034 and reveal the degree of correlation between the datasets. In these correlation plots, each
1035 rectangle is centered on the value of a mean cosmics and x-ray residual pair calculated with a
1036 given tracking combination for every x-ray gun position where data is available. The height
1037 and width of the rectangles are the uncertainty in the mean cosmics and x-ray residuals
1038 respectively. Note that in the scatter plots, the regions of interest where cosmics tracks are
1039 included in the calculation of the mean of residuals are exactly centered on the nominal x-ray
1040 beam positions, unlike in Figure 7.1.

1041 The fitted slope and offset in Figure 7.2 show that the two QL2.P.11 datasets are correlated.
1042 The large uncertainty on the x-ray residuals set a limit on the sensitivity of the analysis,
1043 for if the absolute value of the x-ray residuals of a quadruplet were smaller than the x-ray
1044 residual uncertainties, no conclusion about the correlation could be drawn, as is the case for
1045 layer 2 of sTGC quadruplet QL2.P.8 (Figure 7.3). This result is reflected in the small x-ray
1046 residuals shown in Figure 7.1b that do not reveal a pattern in the relative local offsets across
1047 the surface of sTGC layer 2. However, Figure 7.3 shows that the x-ray and mean cosmics
1048 residuals are clustered approximately around zero as is expected for a quadruplet with small
1049 relative misalignments between layers.

1050 There are three patterns in the residuals on the scatter plot explained by geometry. First,
1051 for both datasets the uncertainty in the extrapolated track residuals were larger than the
1052 interpolated track residuals because of the extrapolation lever arm. For the x-ray residuals,
1053 the effect of the lever arm on the uncertainty was direct since the residual was calculated
1054 from a single straight line; for the mean cosmics residuals it is the widening of the residual
1055 distributions due to the extrapolation lever arm that increases the uncertainty in the fitted
1056 means of residuals. Second, residuals calculated through extrapolation tend to be larger
1057 because the extrapolation lever arm can produce more extreme values of the track position

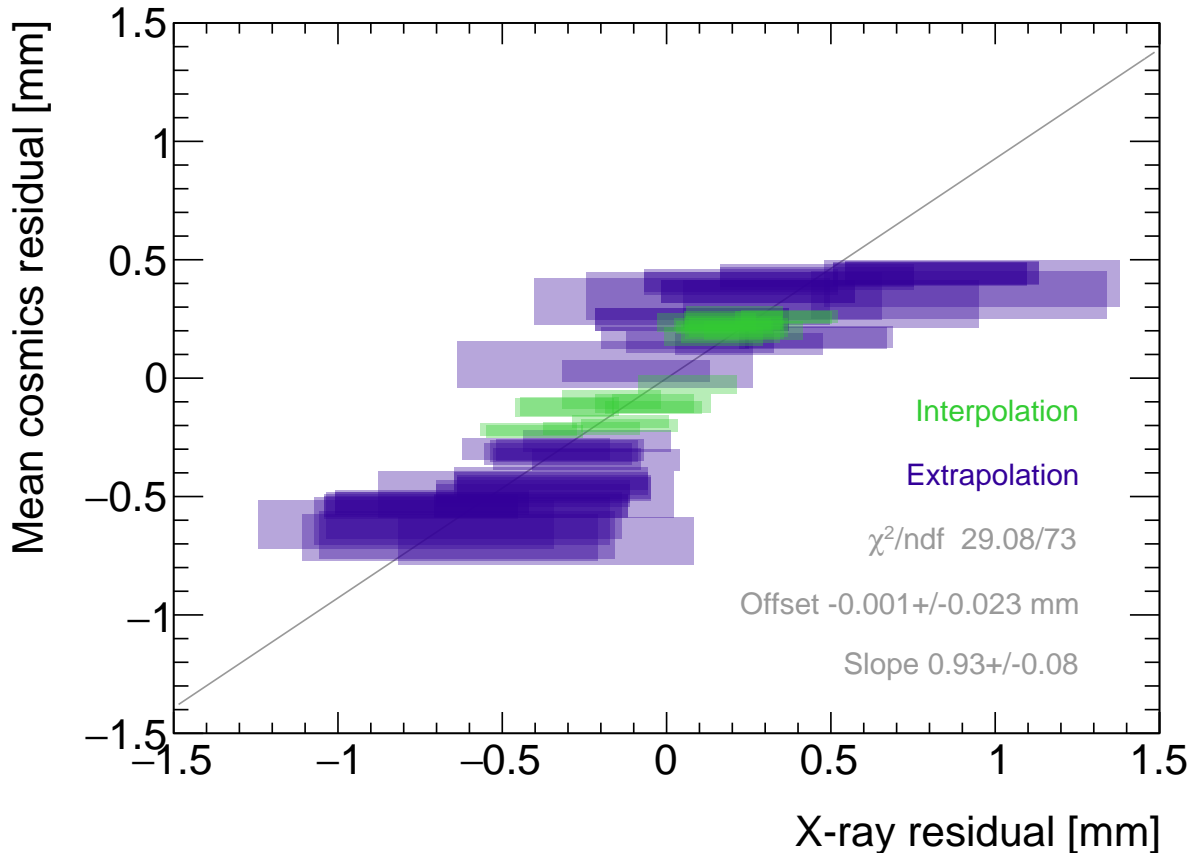


Figure 7.2: Correlation plot between x-ray and mean cosmics residuals for all tracking combinations for QL2.P.11. Each rectangle is centered on an x-ray and mean cosmics residual pair calculated at a given x-ray gun position and for a certain tracking combination. The width of the rectangles in x and y are the uncertainty in the x-ray and mean cosmics residual respectively. A printer-friendly version of this plot is available in Appendix D.

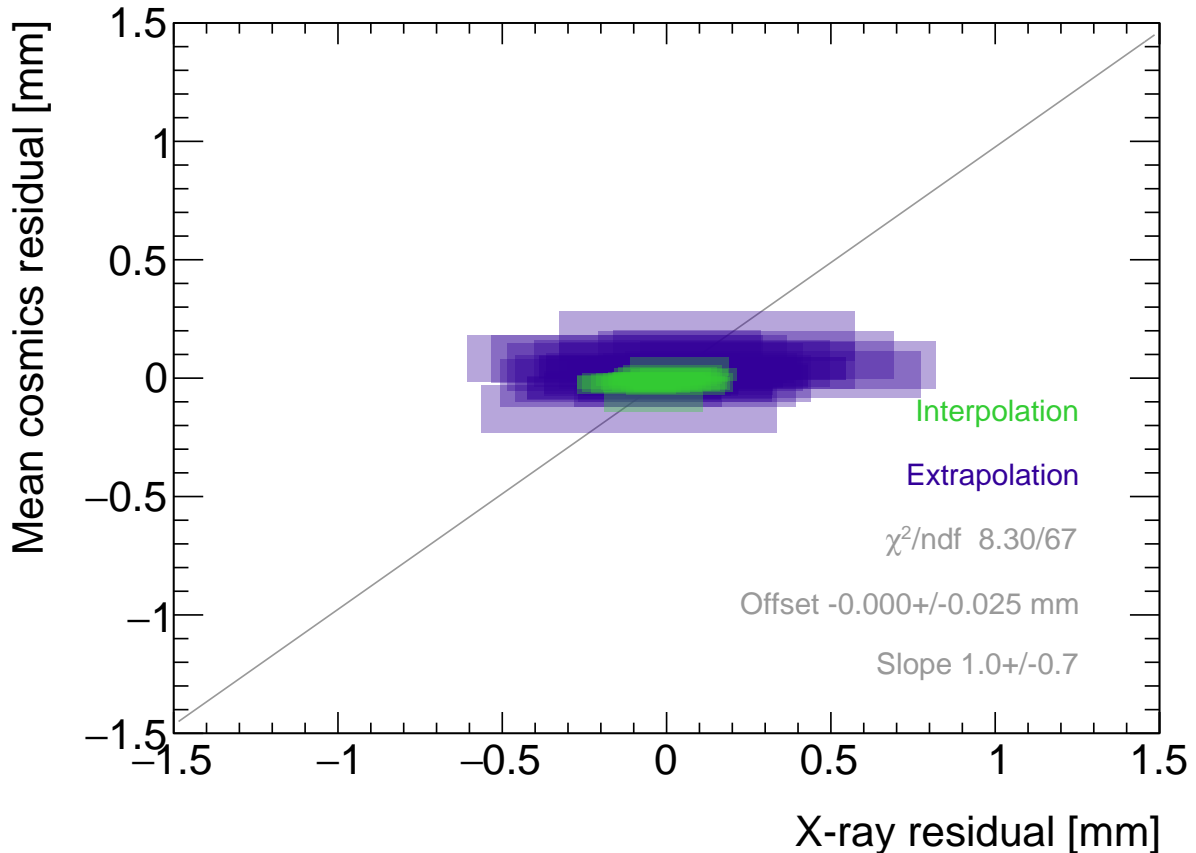


Figure 7.3: Correlation plot between x-ray and mean cosmics residuals for all tracking combinations for QL2.P.8. Each rectangle is centered on an x-ray and mean cosmics residual pair calculated at a given x-ray gun position and for a certain tracking combination. The width of the rectangles in x and y are the uncertainty in the x-ray and mean cosmics residuals respectively. A printer-friendly version of this plot is available in Appendix D.

1058 on the layer of interest. Third, the points in Figure 7.2 are geometrically correlated (e.g.
1059 they seem to be roughly mirrored around the origin). This is expected since the residuals
1060 calculated using a given set of three layers should be geometrically correlated by the local
1061 offsets on each layer (the $d_{local,i}$ on each layer as defined in Equation 5.1).

1062 7.2 Discussion

1063 Several sTGC quadruplets were tested for each quadruplet construction geometry built in
1064 Canada. Each quadruplet fell into one of the two categories: residuals large enough to see
1065 a correlation, or residuals too small to see a correlation. Since the x-ray and mean cosmics
1066 residuals can be used to calculate relative local offsets between the layer and the two reference
1067 layers, quadruplets with the largest relative misalignments had the largest range of residuals.
1068 The correlation plots are another easy visual way to identify quadruplets with large relative
1069 misalignments.

1070 The most significant limit on measuring the degree of correlation between the x-ray and
1071 mean cosmics residuals is the uncertainty on the x-ray residuals, which stemmed from the
1072 systematic uncertainty of 120 μm in the x-ray beam profile centers used to construct the
1073 straight lines. For example, in Figure 7.3, if the x-ray residuals could be known to within
1074 better precision, perhaps they would be correlated with the mean cosmics residuals. The
1075 x-ray method was limited primarily by the systematic uncertainties in the relative alignment
1076 of the alignment platforms and the gun, especially the gun angle.

1077 The analysis of a fraction of the sTGC quadruplets was limited by the availability of data.
1078 Sometimes, less than three sTGC layers in a quadruplet were surveyed for a given x-ray gun
1079 position so no residuals could be calculated. Too few x-ray residuals prevented the analysis
1080 from detecting a significant correlation with cosmics data, should it even be measurable.
1081 Often, the analysis of sTGC quadruplets of smaller sizes (placed innermost on the wheel)
1082 is limited because they have fewer alignment platforms, and hence gun positions, on their
1083 surfaces as a result of their size. The analysis is also limited to a fraction of all sTGC
1084 quadruplets built. The wedges constructed the earliest (typically small wedges) were sur-
1085 veyed when the x-ray method was still being designed, so a limited number of x-ray residuals
1086 can be calculated and the beam profiles were of lower quality.

1087 Nonetheless, the comparison of x-ray and mean cosmics residuals was really to confirm the
1088 x-ray method's ability to measure local offsets with an independent dataset. The x-ray local
1089 offsets allow the calculation of relative local offsets that have been correlated to the cosmics
1090 relative local offsets. Therefore, the analysis of quadruplets with relative local offsets large
1091 enough to detect a correlation validates the x-ray method's ability to measure local offsets.

1092 The potential of using relative local offsets calculated from cosmics data to study relative
 1093 alignment between sTGC layers stands on its own. For example, although the x-ray residuals
 1094 in QL2.P.8 in Figure 7.1b do not reveal a pattern, the variation in the mean cosmics residuals
 1095 do. Identifying the pattern is possible because mean cosmics residuals can be calculated
 1096 across the entire sTGC layer's area and are sensitive to smaller relative local offsets since
 1097 their uncertainty is significantly smaller.

1098 7.3 Next steps

1099 The results presented in this thesis pave the way to the further application of the rich cosmic
 1100 muon data set to alignment work. First, a systematic study of cosmic ray and x-ray relative
 1101 local strip position offsets should be performed for all quadruplets built for the NSWs. The
 1102 correlation plots such as those presented in Figure 7.2 and 7.3 can reveal unexpected results
 1103 which could indicate an issue with either cosmic ray or x-ray data collection to be investigated
 1104 further. Then, the overall correlation between x-ray and cosmic datasets should be quantified
 1105 for all quadruplets instead of being quantified for each quadruplet individually.

1106 For now, the correlation of the individual quadruplets tested supports the use of the x-
 1107 ray data to build an alignment model. The plan is that the alignment parameters will
 1108 be provided to the ATLAS experiment's offline software to estimate the position of each
 1109 strip and so improve precision muon tracks reconstruction using the sTGCs. Work on the
 1110 alignment model is ongoing [8]. Currently, the algorithm compares the offsets of a local
 1111 group of strips at each x-ray gun position as measured by the x-ray and CMM methods
 1112 in a fit to extract a global slope (m) and offset (b) per layer, i , where the χ^2 is given by
 1113 Equation 7.1.

$$\chi^2 = \frac{[dy_{cmm,corr} - dy_{xray}]^2}{\delta dy_{xray}^2 + \delta dy_{cmm,corr}^2}, \quad (7.1)$$

$$dy_{cmm,corr} = y_{cmm} + b_i + m_i x - y_{nom} \quad (7.2)$$

1114
 1115 Here, dy is a local strip position offset as calculated from the x-ray and corrected CMM
 1116 data and δdy refers to their respective uncertainties. The large uncertainty on the x-ray
 1117 local offsets (120 μm) and the sparseness of the measurements means that including input
 1118 from other characterization datasets could reduce the uncertainty on the alignment model
 1119 parameters.

1120 Work on adding the relative local strip position offsets measured using cosmic ray data to the
1121 alignment model has begun. They provide alignment information between the x-ray measure-
1122 ment points and can be calculated with a precision relevant to alignment studies. Therefore,
1123 they provide additional and complementary information that could further constrain the
1124 global rotation and translation parameter of the simple misalignment model currently being
1125 used. It is compelling to imagine improving the accuracy of the alignment model given that
1126 the accuracy to which the positions of the strips are known in ATLAS will affect the quality
1127 of the reconstructed muon tracks used to study high energy physics processes.

₁₁₂₈

Chapter 8

₁₁₂₉

Summary and outlook

₁₁₃₀ The LHC [1] will be at the energy frontier of particle physics for at least the next decade,
₁₁₃₁ making it a unique tool with which to study particle physics. With the HL-LHC [2], high
₁₁₃₂ statistics on rare particle physics processes will enable more precise measurements of pa-
₁₁₃₃ rameters of the Standard Model and increase the sensitivity to signatures of physics beyond
₁₁₃₄ the Standard Model [3]. To capitalize on the increased luminosity, the muon small wheels
₁₁₃₅ of the ATLAS experiment must be replaced to keep the current triggering and tracking
₁₁₃₆ performance [5].

₁₁₃₇ sTGCs are gas ionization chambers optimized for a high rate environment [5]. Using the pad
₁₁₃₈ electrodes to define a region of interest makes it possible to get track segments of ~ 1 mrad
₁₁₃₉ angular resolution quickly, which will be used as input to check if a collision originated
₁₁₄₀ from the interaction point and whether it should be triggered on [5, 53]. Thanks to the
₁₁₄₁ careful design of the sTGCs, particularly the small pitch of the strip readout electrodes, the
₁₁₄₂ sTGCs are able to provide better than $100 \mu\text{m}$ position resolution per detector plane to fulfill
₁₁₄₃ precision offline tracking requirements [6].

₁₁₄₄ Ultimately, the positions of the sTGC strip electrodes need to be known in ATLAS to within
₁₁₄₅ $\sim 100 \mu\text{m}$ so that they can deliver the required position resolution [5]. The strategy is to build
₁₁₄₆ an alignment model to estimate the position of each strip [8]. Input to the alignment model
₁₁₄₇ comes from the datasets used to characterize the quadruplets. The x-ray data [8] is the only
₁₁₄₈ characterization dataset that directly links the position of the strips to the ATLAS coordinate
₁₁₄₉ system. The alignment model could be built on x-ray data alone, but the sparseness of and
₁₁₅₀ large uncertainty on the local offsets mean that the alignment model could benefit from more
₁₁₅₁ input. The x-ray method is also a new technique that should be independently validated.

₁₁₅₂ Relative local offsets measured with the cosmics and x-ray datasets were compared and the
₁₁₅₃ observed correlation confirmed the local offsets measured with the x-ray gun. Moreover, the

1154 cosmics relative local offsets are useful on their own. The 2D visualizations of relative local
1155 offsets make it possible to quickly identify areas of misaligned strips and make hypotheses as
1156 to the physical origin of those misalignments. Also, the cosmics residual means were shown
1157 to be robust and have uncertainties under 100 μm for all two-fixed-layer reference frames,
1158 which is small in this context. Therefore, the cosmics relative local offsets complement the x-
1159 ray data by providing a complete, robust picture of the relative strip position offsets between
1160 layers. The next goal will be to use the cosmics relative local offsets to improve the alignment
1161 model and better position the sTGC strips in ATLAS.

1162 Muons are important signatures of electroweak and Higgs sector events that physicists an-
1163 ticipate studying with a high-statistics dataset [3, 5]. An effective alignment model of sTGC
1164 strip positions will ensure that the NSWs can be used to accomplish the ATLAS collabora-
1165 tion’s physics goals during the High Luminosity era of the LHC.

¹¹⁶⁶ References

- ¹¹⁶⁷ [1] L. Evans and P. Bryant. LHC Machine. *Journal of Instrumentation*, 3(S08001), August
¹¹⁶⁸ 2008.
- ¹¹⁶⁹ [2] G. Apollinari et al. High-Luminosity Large Hadron Collider (HL-LHC) Technical Design
¹¹⁷⁰ Report V. 0.1. Technical Report CERN-2017-007-M, CERN, Geneva, September 2017.
- ¹¹⁷¹ [3] A. Dainese et al. The physics potential of HL-LHC. In *Input to the European Particle
1172 Physics Strategy Update*, November 2018.
- ¹¹⁷³ [4] The ATLAS Collaboration. The ATLAS Experiment at the CERN Large Hadron Col-
¹¹⁷⁴ linder. *Journal of Instrumentation*, 3(08):S08003, August 2008.
- ¹¹⁷⁵ [5] T. Kawamoto et al. New Small Wheel Technical Design Report. Technical Report
¹¹⁷⁶ CERN-LHCC-2013-006, ATLAS-TDR-020, CERN, Geneva, June 2013.
- ¹¹⁷⁷ [6] A. Abusleme et al. Performance of a Full-Size Small-Strip Thin Gap Chamber Prototype
¹¹⁷⁸ for the ATLAS New Small Wheel Muon Upgrade. *Nuclear Instruments and Methods in
1179 Physics Research Section A: Accelerators, Spectrometers, Detectors and Associated
1180 Equipment*, 817:85–92, May 2016. arXiv: 1509.06329.
- ¹¹⁸¹ [7] E.M. Carlson. *Results of the 2018 ATLAS sTGC test beam and internal strip alignment
1182 of sTGC detectors*. M.Sc. thesis, University of Victoria, Victoria, Canada, 2019.
- ¹¹⁸³ [8] B. Lefebvre. Precision survey of the readout strips of small-strip Thin Gap Chambers
¹¹⁸⁴ using X-rays for the muon spectrometer upgrade of the ATLAS experiment. *Journal of
1185 Instrumentation*, 15(07):C07013–C07013, July 2020.
- ¹¹⁸⁶ [9] D.J. Griffiths. *Introduction to elementary particles*. Physics textbook. Wiley-VCH,
¹¹⁸⁷ Weinheim, Germany, 2., rev. ed., 5. reprint edition, 2011.
- ¹¹⁸⁸ [10] M.E. Peskin and D.V. Schroeder. *An introduction to quantum field theory*. Addison-
¹¹⁸⁹ Wesley Pub. Co, Reading, Massachusetts, 1995.

- 1190 [11] P.A. Zyla et al. Review of Particle Physics. *PTEP*, 2020(8):083C01, 2020.
- 1191 [12] M. Kobayashi and T. Maskawa. CP-violation in the renormalizable theory of weak
1192 interaction. *Progress of theoretical physics*, 49(2):652–657, February 1973.
- 1193 [13] M.L. Perl et al. Evidence for Anomalous Lepton Production in $\{e\}^{\{+}\backslash\text{ensuremath}{-}\}$
1194 $\{e\}^{\{\backslash\text{ensuremath}{-}\}}\}$ Annihilation. *Physical Review Letters*, 35(22):1489–1492, De-
1195 cember 1975. Publisher: American Physical Society.
- 1196 [14] F. Englert and R. Brout. Broken Symmetry and the Mass of Gauge Vector Mesons.
1197 *Physical Review Letters*, 13(9):321–323, August 1964. Publisher: American Physical
1198 Society.
- 1199 [15] P.W. Higgs. Broken symmetries, massless particles and gauge fields. *Physics Letters*,
1200 12(2):132–133, September 1964.
- 1201 [16] D. Galbraith and C. Burgard. UX: Standard Model of the Stan-
1202 dard Model, November 2013. [http://davidgalbraith.org/portfolio/
1203 ux-standard-model-of-the-standard-model/](http://davidgalbraith.org/portfolio/ux-standard-model-of-the-standard-model/) last accessed on 2021-09-30.
- 1204 [17] C.A. Bertulani. *Nuclear physics in a nutshell*. In a nutshell. Princeton University Press,
1205 Princeton, N.J, 2007. OCLC: ocm85690422.
- 1206 [18] B.W. Carroll and D.A. Ostlie. *An introduction to modern astrophysics*. Pearson
1207 Addison-Wesley, San Francisco, 2nd ed edition, 2007. OCLC: ocm69020924.
- 1208 [19] M. Boezio and E. Mocchiutti. Chemical composition of galactic cosmic rays with space
1209 experiments. *Astroparticle Physics*, 39-40:95–108, December 2012.
- 1210 [20] The SNO Collaboration. Combined analysis of all three phases of solar neutrino data
1211 from the sudbury neutrino observatory. *Phys. Rev. C*, 88:025501, August 2013.
- 1212 [21] B. Pontecorvo. Neutrino Experiments and the Problem of Conservation of Leptonic
1213 Charge. *Soviet Physics—JETP*, 53:1717–1725, 1967.
- 1214 [22] S.M. Bilenky and S.T. Petcov. Massive neutrinos and neutrino oscillations. *Reviews of
1215 Modern Physics*, 59(3):671–754, July 1987.
- 1216 [23] B. Young. A survey of dark matter and related topics in cosmology. *Frontiers of Physics*,
1217 12(2):121201, April 2017.
- 1218 [24] C. Muñoz. Dark matter detection in the light of recent experimental results. *International
1219 Journal of Modern Physics A*, 19(19):3093–3169, July 2004.

- 1220 [25] G. Arnison et al. Experimental observation of isolated large transverse energy elec-
1221 trons with associated missing energy at s=540 GeV. *Physics Letters B*, 122(1):103–116,
1222 February 1983.
- 1223 [26] M. Banner et al. Observation of single isolated electrons of high transverse momentum
1224 in events with missing transverse energy at the CERN pp collider. *Physics Letters B*,
1225 122(5):476–485, March 1983.
- 1226 [27] G. Arnison et al. Experimental observation of lepton pairs of invariant mass around 95
1227 GeV/c² at the CERN SPS collider. *Physics Letters B*, 126(5):398–410, July 1983.
- 1228 [28] P. Bagnaia et al. Evidence for Z → e⁺e⁻ at the CERN pp collider. *Physics Letters B*,
1229 129(1):130–140, 1983.
- 1230 [29] The CDF Collaboration. Observation of Top Quark Production in $\bar{p}p$ Collisions with
1231 the Collider Detector at Fermilab. *Physical Review Letters*, 74(14):2626–2631, April
1232 1995. Publisher: American Physical Society.
- 1233 [30] The D0 Collaboration. Observation of the Top Quark. *Physical Review Letters*,
1234 74(14):2632–2637, April 1995. Publisher: American Physical Society.
- 1235 [31] The ATLAS Collaboration. Observation of a new particle in the search for the Standard
1236 Model Higgs boson with the ATLAS detector at the LHC. *Physics Letters B*, 716(1):1–
1237 29, September 2012. arXiv: 1207.7214.
- 1238 [32] The CMS Collaboration. Observation of a new boson at a mass of 125 GeV with the
1239 CMS experiment at the LHC. *Physics Letters B*, 716(1):30–61, September 2012. arXiv:
1240 1207.7235.
- 1241 [33] Standard Model Summary Plots June 2021, June 2021. <https://atlas.web.cern.ch/Atlas/GROUPS/PHYSICS/PUBNOTES/ATL-PHYS-PUB-2021-032/> last accessed on 2021-
1242 09-30.
- 1243 [34] O.S. Brüning et al. LHC Design Report. Design Report CERN-2004-003-V-1, CERN,
1244 CERN, Geneva, Switzerland, 2004. ISBN: 9789290832249.
- 1245 [35] ATLAS luminosity public results run-1, March 2011. <https://twiki.cern.ch/twiki/bin/view/AtlasPublic/LuminosityPublicResults> last accessed on 2021-09-20.
- 1246 [36] ATLAS luminosity public results run-2, July 2015. <https://twiki.cern.ch/twiki/bin/view/AtlasPublic/LuminosityPublicResultsRun2> last accessed on 2021-09-20.

- 1250 [37] The European Strategy for Particle Physics. Technical Report CERN/2685, CERN,
1251 2006. Adopted by the CERN council at a special session at ministerial level in Lisbon
1252 in 2006.
- 1253 [38] HiLumi HL-LHC Project. LHC/HL-LHC plan (last update january 2021). <https://hilumilhc.web.cern.ch/content/hl-lhc-project>, last accessed on 2021-09-09.
- 1255 [39] M. Cepeda et al. Report from Working Group 2: Higgs Physics at the HL-LHC and
1256 HE-LHC. In A. Dainese et al., editors, *Report on the Physics at the HL-LHC, and*
1257 *Perspectives for the HE-LHC*, number CERN-LPCC-2018-04, pages 221–584. 364 p,
1258 CERN, Geneva, Switzerland, Jun 2018. CERN.
- 1259 [40] ATLAS inner detector : Technical Design Report, 1. Technical Report CERN-LHCC-
1260 97-016, CERN, April 1997. ISBN: 9789290831020 Publication Title: CERN Document
1261 Server.
- 1262 [41] S. Haywood, L. Rossi, R. Nickerson, and A. Romanouk. ATLAS inner detector :
1263 Technical Design Report, 2. Technical Report CERN-LHCC-97-017, CERN, April 1997.
1264 ISBN: 9789290831037 Publication Title: CERN Document Server.
- 1265 [42] C. Grupen, B.A. Shwartz, and H. Spieler. *Particle detectors*. Cambridge University
1266 Press, Cambridge, UK; New York, 2008. OCLC: 1105536566.
- 1267 [43] ATLAS liquid-argon calorimeter : Technical Design Report. Technical Report CERN-
1268 LHCC-96-041, CERN, 1996. ISBN: 9789290830900 Publication Title: CERN Document
1269 Server.
- 1270 [44] ATLAS tile calorimeter : Technical Design Report. Technical Report CERN-LHCC-96-
1271 042, CERN, 1996. ISBN: 9789290830917 Publication Title: CERN Document Server.
- 1272 [45] The ATLAS Collaboration. ATLAS Muon Spectrometer: Technical Design Report.
1273 Technical Report CERN-LHCC-97-022, CERN, Geneva, 1997.
- 1274 [46] ATLAS magnet system : Technical Design Report, 1. Technical Report CERN-LHCC-
1275 97-018, CERN, April 1997. ISBN: 9789290831044 Publication Title: CERN Document
1276 Server.
- 1277 [47] The ATLAS Collaboration. Performance of the ATLAS muon trigger in pp collisions
1278 at $\sqrt{s} = 8$ TeV. *The European Physical Journal C*, 75(3):120, March 2015. arXiv:
1279 1408.3179.

- 1280 [48] S. Aefsky et al. The Optical Alignment System of the ATLAS Muon Spectrometer End-
1281 caps. *Journal of Instrumentation*, 3(11):P11005–P11005, November 2008. Publisher:
1282 IOP Publishing.
- 1283 [49] ATLAS level-1 trigger : Technical Design Report. Technical Report CERN-LHCC-98-
1284 014, CERN, August 1998. ISBN: 9789290831280 Publication Title: CERN Document
1285 Server.
- 1286 [50] A. Ruiz Martínez. The run-2 ATLAS trigger system. *Journal of Physics: Conference
1287 Series*, 762:012003, October 2016.
- 1288 [51] Technical Design Report for the Phase-II Upgrade of the ATLAS TDAQ System. Tech-
1289 nical Report CERN-LHCC-2017-020, ATLAS-TDR-029, CERN, Geneva, September
1290 2017.
- 1291 [52] P. Jenni, M. Nessi, M. Nordberg, and K. Smith. ATLAS high-level trigger, data-
1292 acquisition and controls : Technical Design Report. Technical Report CERN-LHCC-
1293 2003-022, CERN, July 2003.
- 1294 [53] E. Perez Codina. Small-strip Thin Gap Chambers for the muon spectrometer upgrade of
1295 the ATLAS experiment. *Nuclear Instruments and Methods in Physics Research Section
1296 A: Accelerators, Spectrometers, Detectors and Associated Equipment*, 824:559–561, July
1297 2016.
- 1298 [54] J. Townsend. *Electricity in gases*. Clarendon Press, Oxford, 1915.
- 1299 [55] S. Majewski, G. Charpak, A. Breskin, and G. Mikenberg. A thin multiwire chamber
1300 operating in the high multiplication mode. *Nuclear Instruments and Methods*, 217:265–
1301 271, 1983.
- 1302 [56] E. Gatti, A. Longoni, H. Okuno, and P. Semenza. Optimum geometry for strip cathodes
1303 or grids in MWPC for avalanche localization along the anode wires. *Nuclear Instruments
1304 and Methods*, 163(1):83–92, July 1979.
- 1305 [57] G. Battistoni et al. Resistive cathode transparency. *Nuclear Instruments and Methods
1306 in Physics Research*, 202(3):459–464, November 1982.
- 1307 [58] B. Lefebvre. *Characterization studies of small-strip Thin Gap Chambers for the ATLAS
1308 Upgrade*. PhD thesis, McGill University, Montreal, Canada, 2018.
- 1309 [59] P.K.F. Grieder. *Cosmic rays at Earth: researcher’s reference manual and data book*.
1310 Elsevier Science Ltd, Amsterdam, 1st ed edition, 2001.

- 1311 [60] R. Keyes et al. Development and characterization of a gas system and its associated
 1312 slow-control system for an ATLAS small-strip thin gap chamber testing facility. *Journal*
 1313 *of Instrumentation*, 12(04):P04027–P04027, April 2017.
- 1314 [61] Georgios Iakovidis. VMM3, an ASIC for Micropattern Detectors. Technical Report
 1315 ATL-MUON-PROC-2018-003, CERN, Geneva, March 2018.
- 1316 [62] B. Chen. *Calibration Studies of the Front-End Electronics for the ATLAS New Small*
 1317 *Wheel Project*. M.Sc. thesis, McGill University, Montreal, Canada, 2019.
- 1318 [63] R. Brun and F. Rademakers. ROOT: An object oriented data analysis framework. *Nu-*
 1319 *clear Instruments and Methods in Physics Research Section A: Accelerators, Spectrome-*
 1320 *ters, Detectors and Associated Equipment*, 389:81–86, 1997. See also ”ROOT” [software],
 1321 Release 6.18/02, 23/08/2019, (<https://zenodo.org/record/3895860#.YVJW6n0pCHs>).
- 1322 [64] F. Sauli. Principles of operation of multiwire proportional and drift chambers. Number 81 in CERN Academic Training Lectures, CERN, Geneva, Switzerland, September
 1323 1975 – June 1976. CERN.
- 1325 [65] M. Hatlo et al. Developments of mathematical software libraries for the LHC experi-
 1326 ments. *IEEE Transactions on Nuclear Science*, 52:2818–2822, 2005.
- 1327 [66] H. Guo. A Simple Algorithm for Fitting a Gaussian Function [DSP Tips and Tricks].
 1328 *IEEE Signal Processing Magazine*, 28(5):134–137, September 2011.
- 1329 [67] I. Endo et al. Systematic shifts of evaluated charge centroid for the cathode read-out
 1330 multiwire proportional chamber. *Nuclear Instruments and Methods in Physics Research*,
 1331 188(1):51–58, September 1981.
- 1332 [68] Minature x-ray source mini-x. Product of Amptek Inc. <https://www.amptek.com/-/media/ametekamptek/documents/resources/specs/mini-x-specifications.pdf?la=en&revision=512f7eb3-01b3-47fd-864f-5525c850fc6e&hash=B8B03C0592486E2D91C566C4326F15F5>, last accessed on 2021-10-15.
- 1336 [69] B. Stelzer. The New Small Wheel Upgrade Project of the ATLAS Experiment. *Nuclear*
 1337 *and Particle Physics Proceedings*, 273-275:1160–1165, April 2016.
- 1338 [70] X. Zhao et al. Cosmic test of sTGC detector prototype made in China for ATLAS
 1339 experiment upgrade. *Nuclear Instruments and Methods in Physics Research Section A:*
 1340 *Accelerators, Spectrometers, Detectors and Associated Equipment*, 927:257–261, May
 1341 2019.

¹³⁴² APPENDICES

₁₃₄₃ **Appendix A**

₁₃₄₄ **Uncertainty in cluster positions**

₁₃₄₅ The clusters were fit with Guo's method [66] and Minuit2 for ROOT [65]. The difference in
₁₃₄₆ cluster means between the two algorithms is shown in Figure A.1.

₁₃₄₇ The RMS of the distribution in Figure A.1 is 57 μm , which is much larger than the sta-
₁₃₄₈ tistical uncertainty in the mean for the Minuit2 algorithm, which peaks around 7 μm . An
₁₃₄₉ RMS of 60 μm is common for data taken with most quadruplets at 3.1 kV. Therefore, the
₁₃₅₀ uncertainty in the reconstructed cluster y -coordinate is assigned 60 μm due to variations in
₁₃₅₁ the reconstruction with different Gaussian fit algorithms.

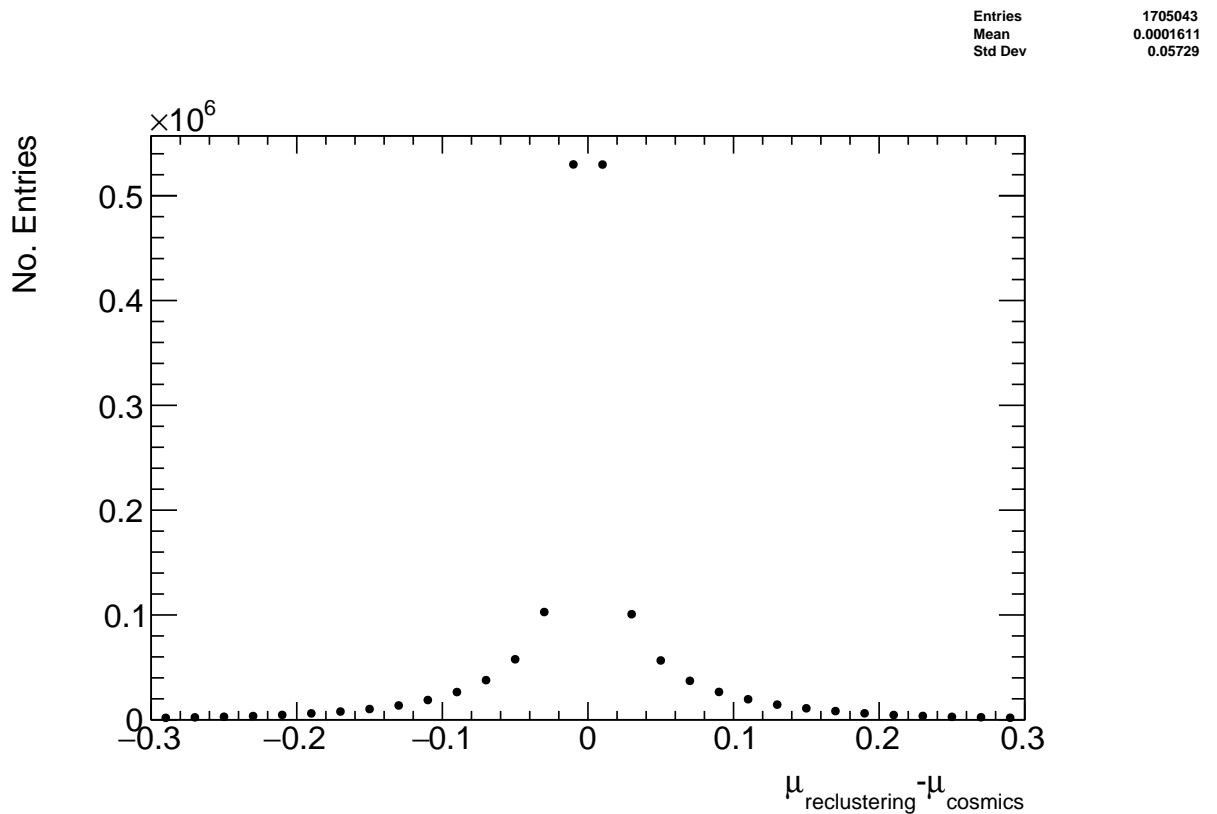


Figure A.1: The difference between cluster means calculated with Guo's method [66] in `tgc_analysis/CosmicsAnalysis` and Minuit2 for ROOT [65] in `strip_position_analysis/ReClustering` for data collected with QL2.P.8 at 3.1 kV.

1352 **Appendix B**

1353 **Study of cosmics for alignment
1354 analysis statistical uncertainty**

1355 Typically, one million triggers (cosmic muon events, noise, photons and δ -rays) were collected
1356 for each Canadian quadruplet at McGill University, resulting in roughly half the number of
1357 viable tracks after cuts. For QS3.P.18, 3.5 million triggers were collected. To gauge the
1358 sensitivity of the analysis to the available statistics, partitions of this data with each with
1359 a different number of triggers were analyzed separately. Ultimately, the quantity of interest
1360 was the Gaussian mean of the residual distribution in regions of interest, so the peak in the
1361 distribution of the statistical uncertainty in the residual means for each area of interest for
1362 a specific tracking combination was used to gauge the quality of the analysis. How the peak
1363 in the residual mean uncertainty distribution changes with the number of triggers is shown
1364 in Figure B.1 for tracks on layer 1 built from layers 3 and 4.

1365 The uncertainty is already around 20 μm at 1 million triggers, suitable for distinguishing
1366 differences in offsets of order 50 μm as required. Although increased statistics could decrease
1367 the statistical uncertainty, it is not required for the goals of this analysis. Moreoever, the
1368 systematic uncertainty on the mean cosmics residuals is around 50 μm so the statistical
1369 uncertainty of 20 μm is nearly negligible.

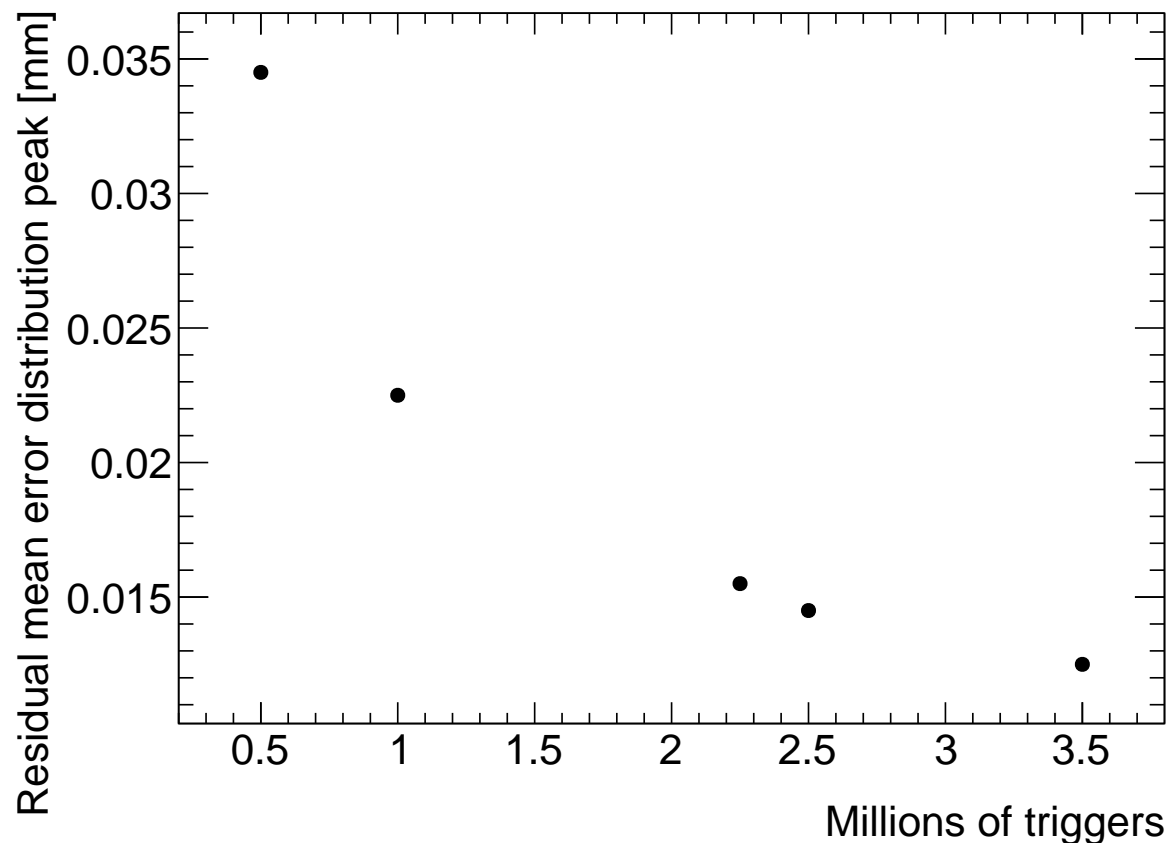


Figure B.1: How the peak of the distributions of uncertainties in the residual means in regions of interest for tracks on layer 1 built from layers 3 and 4 changed with the number of triggers used in the analysis. The distribution falls off as $\frac{1}{\sqrt{N}}$ as expected.

¹³⁷⁰ Appendix C

¹³⁷¹ Study of systematic uncertainties ¹³⁷² when using cosmics data for ¹³⁷³ alignment studies

¹³⁷⁴ C.1 Residual distribution fit function

¹³⁷⁵ The distribution of residuals should be modeled by a double Gaussian fit[58]:

$$G(r) = A_s \exp\left[\frac{-(r - \mu)^2}{2\sigma_s^2}\right] + A_b \exp\left[\frac{-(r - \mu)^2}{2\sigma_b^2}\right] \quad (\text{C.1})$$

¹³⁷⁶ where r is the residual, A is the Gaussian amplitude, μ is the Gaussian mean, σ is the
¹³⁷⁷ Gaussian sigma, and the subscripts s and b stand for signal and background respectively.
¹³⁷⁸ One Gaussian captures the real (signal) tracks and the other captures the tracks built from
¹³⁷⁹ noise (background). The Gaussian with the smaller width is identified as the signal.

¹³⁸⁰ A single Gaussian fit failed less often than a double Gaussian fit. The Gaussian fits were
¹³⁸¹ performed by initially estimating the amplitude to be 100 tracks, the Gaussian mean to be
¹³⁸² the histogram mean, and Gaussian σ to be the RMS. The fit range was restricted to ± 1
¹³⁸³ root-mean-square (RMS) from the histogram mean. The modification helped the Gaussian
¹³⁸⁴ fit capture the signal peak. An example residual distribution is shown in Figure C.1.

¹³⁸⁵ For all residual distributions in 100 mm by 100 mm bins on layer 4 built from clusters on
¹³⁸⁶ layers 1 and 2, the difference in Gaussian and double Gaussian means and σ 's is shown in
¹³⁸⁷ Figure C.2a. The mean of the distribution is centered around zero (within the RMS of the

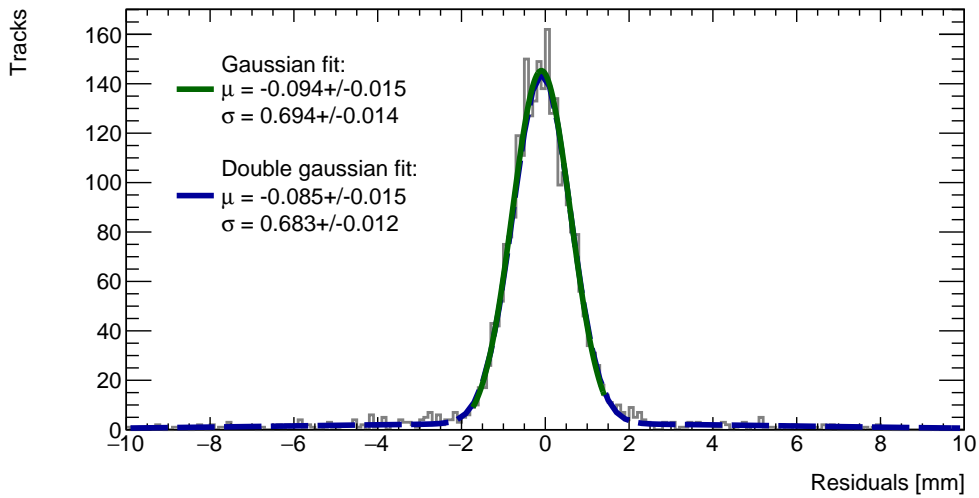
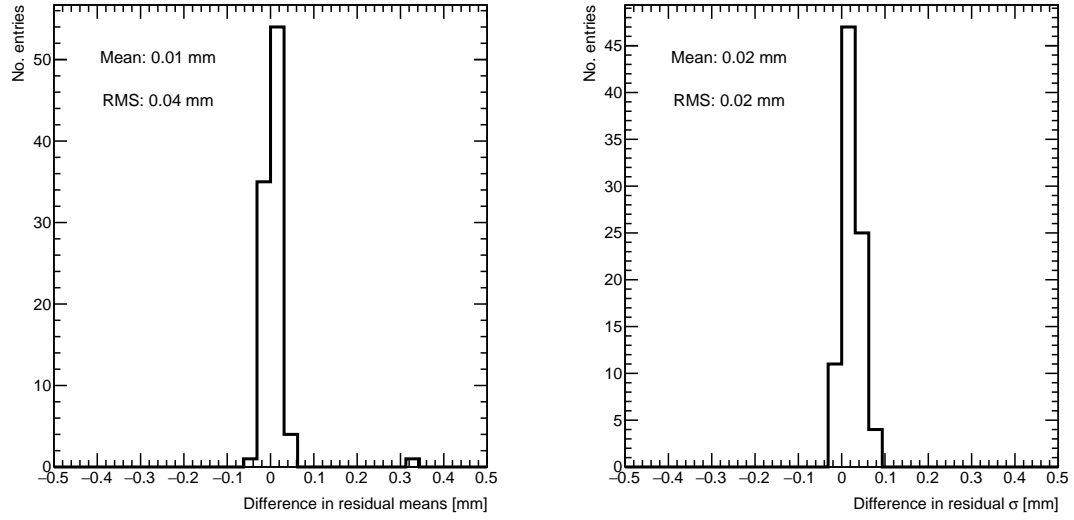


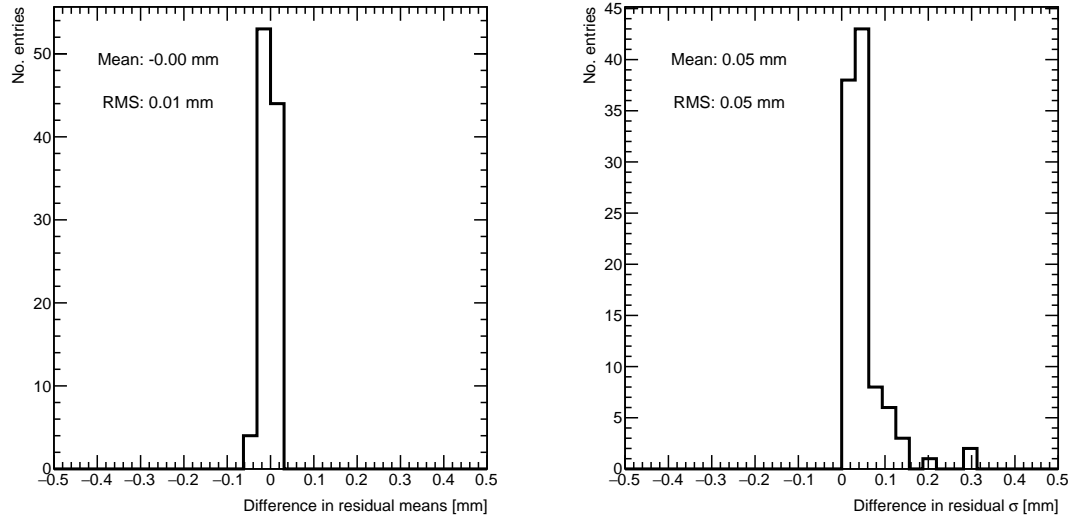
Figure C.1: Residual distribution for track residuals on layer 4 built from clusters on layers 1 and 2 for $x \in [-3.00, 97.00]$ mm, $y \in [394.60, 494.60]$ mm, fit with a double Gaussian and a single Gaussian in a range of ± 1 RMS from the histogram mean.

1388 distribution) so the choice of fit algorithm imbues no measurable bias. The order of the
1389 RMS is such that the difference in residual means at 40 μm is just significant, so it should
1390 be accounted for as a systematic uncertainty on the Gaussian residual means. The 40 μm
1391 RMS is for the tracking combination with the worst extrapolation lever arm and the widest
1392 distribution of mean differences; the interpolation combinations have narrower distributions,
1393 as shown in Figure C.2b. The RMS of the distribution for residual means on layer 2 obtained
1394 using reference layers 1 and 3 is only 10 μm , which is almost negligible.

1395 The Gaussian σ should be larger than the double Gaussian σ because the Gaussian distri-
1396 bution includes the effect of the noise tracks that can yield large residuals, while the double
1397 Gaussian models signal and background residuals separately. For this analysis, only the
1398 residual mean was important, so the systematic overestimate of the signal σ in the Gaussian
1399 fit shown in the right-side plots of Figure C.2 was allowed.



(a) Difference in residual distribution means (left) and σ 's (right) extracted with a Gaussian and double Gaussian fit, for all residual distributions in 100 mm by 100 mm bins on layer 4 built from clusters on layers 1 and 2 for sample quadruplet QL2.P.8.



(b) Difference in residual distribution means (left) and σ 's (right) for a Gaussian and double Gaussian fit, for all residual distributions in 100 mm by 100 mm bins on layer 2 built from clusters on layers 1 and 3 for sample quadruplet QL2.P.8.

Figure C.2

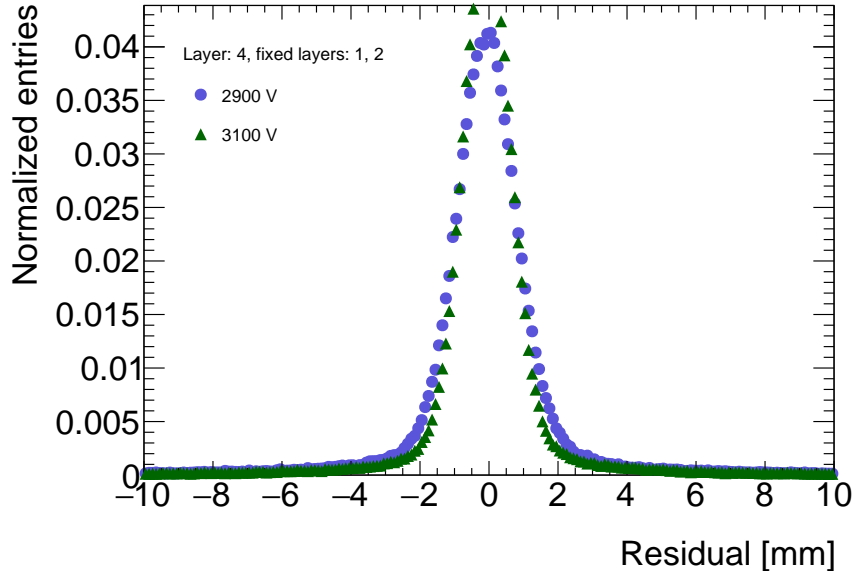


Figure C.3: Residual distribution for tracks on layer 4 built from clusters on layers 1 and 2 for sample quadruplet QL2.P.8 for data collected at 2.9 kV and 3.1 kV.

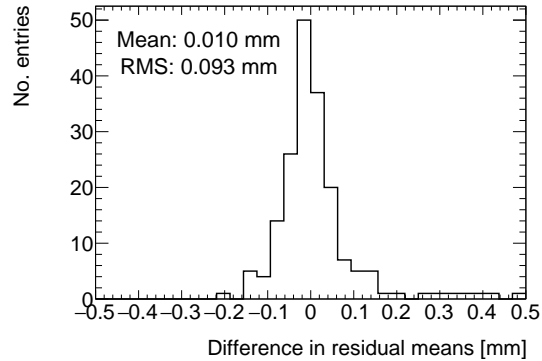
1400 Ultimately, a Gaussian fit was chosen for the track residual distributions because it was more
1401 robust and did not affect the fitted mean values too strongly.

1402 C.2 Cosmic muon data collection voltage

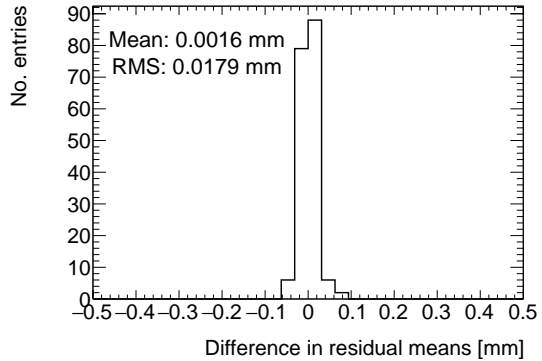
1403 Cosmic muon data was collected at 2.9 kV and 3.1 kV because although 2.9 kV is closer to
1404 the operating conditions the chambers will be subject to in ATLAS, the extra gain provided
1405 by operating at 3.1 kV increased the signal to noise ratio for pad signals. Also, the tracking
1406 efficiency was higher with data collected at 3.1 kV. As such, cosmic muon data collected at
1407 3.1 kV was used in the analysis presented in the body of the thesis.

1408 The difference in gain affects the relative population of clusters of different sizes, which in
1409 turn affects the uncertainty in the mean cluster positions on each layer, the uncertainty in
1410 the track positions and the residual distributions. The residual distributions for 3.1 kV data
1411 are narrower, as shown in Figure C.3.

1412 Neither dataset is better for calculating the mean of residuals in a given area, so a systematic
1413 uncertainty can be assigned based on the difference in residual means calculated for 2.9 kV
1414 and 3.1 kV data per tracking combination. For each tracking combination, the difference



(a) Difference in residual means when measured with residuals on layer 4 built from clusters on layers 1 and 2.



(b) Difference in residual means when measured with residuals on layer 2 built from clusters on layers 1 and 3.

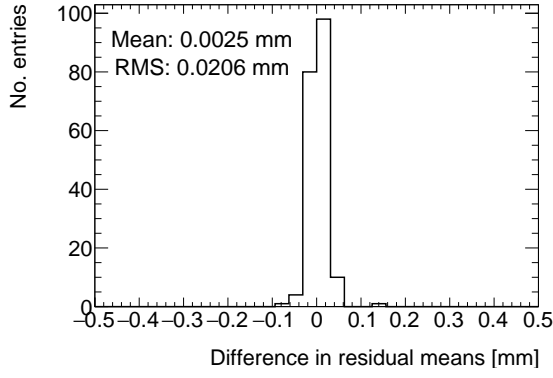
Figure C.4: Difference in residual means for data collected with sample quadruplet QL2.P.8 at 2.9 kV and 3.1 kV respectively in 100 mm by 100 mm bins.

1415 in the fitted track residual means in 100 mm by 100 mm areas for 2.9 kV and 3.1 kV data
 1416 are put in a distribution for a sample quadruplet, as shown in Figure C.4. The means of
 1417 the distributions for both tracking combinations are near zero, so as expected the collection
 1418 voltage introduces no bias. Tracks built from clusters on layers 1 and 2 and extrapolated to
 1419 layer 4 have the worst lever arm and hence the largest root-mean-square (RMS) of 100 μm .
 1420 The width of the distributions for geometrically favourable tracking combinations are much
 1421 narrower. The narrowest width of the residual mean difference distribution is for tracks on
 1422 layer 2 built from clusters on layers 1 and 3 (see Figure C.4b), with a value of 20 μm .

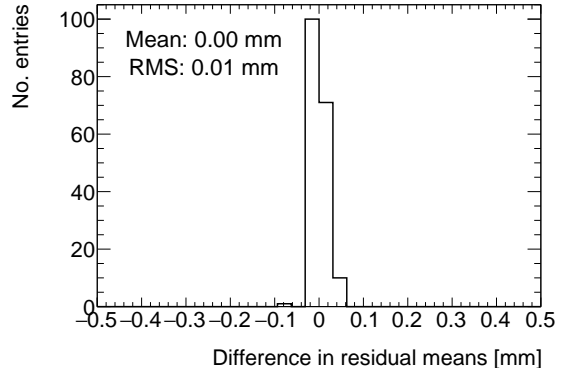
1423 C.3 Cluster fit algorithm

1424 To ensure that changing the cluster fitting algorithm like in Appendix A would not change
 1425 the calculated mean of residuals in each region of interest significantly, the residual means
 1426 were compared in both cases. The distribution of the difference in residual means is plotted
 1427 in Figure C.5 for the tracking combinations with the worst and most favourable extrapolation
 1428 lever arms.

1429 The mean of the distributions are centered around zero, so the choice of cluster fit algorithm
 1430 did not introduce any bias. Differences on the order of 50 μm are important, so the root-
 1431 mean-squares (RMS's) of the distributions show that the clustering algorithm had a small
 1432 but notable effect between 10-20 μm from the most to least geometrically favourable tracking



(a) Difference in residual means when measured with residuals on layer 4 built from clusters on layers 1 and 2.



(b) Difference in residual means when measured with residuals on layer 2 built from clusters on layers 1 and 3.

Figure C.5: Difference in residual means when the cluster fit algorithm is `Minuit2` [65] versus Guo's method [66] for two different tracking combinations for sample quadruplet, QL2.P.8.

1433 combinations. Therefore, the RMS for each tracking combination will be used to add a
 1434 systematic uncertainty on the residual means accounting for the effect that different cluster
 1435 fit algorithms have on the residual means.

1436 C.4 Differential non-linearity

1437 Definition

1438 In this context, differential non-linearity (DNL) is when the reconstructed cluster mean is
 1439 biased by the fit of the discretely sampled peak signal amplitude distribution over the strips.
 1440 The bias depends on the relative position of the avalanche with respect to the center of the
 1441 closest strip. For a summary of DNL, refer to page 40 of [58], an early paper studying its
 1442 effects [67], and for an example application, refer to [6].

1443 Application and effect of DNL

1444 The cluster mean was corrected for DNL using the equation:

$$y' = y + a \sin(2\pi y_{rel}) \quad (\text{C.2})$$

1445 where y is the cluster mean, y_{rel} is the relative position of the cluster mean with respect
 1446 to the strip's center, a is the amplitude of the correction, and y' is the corrected cluster

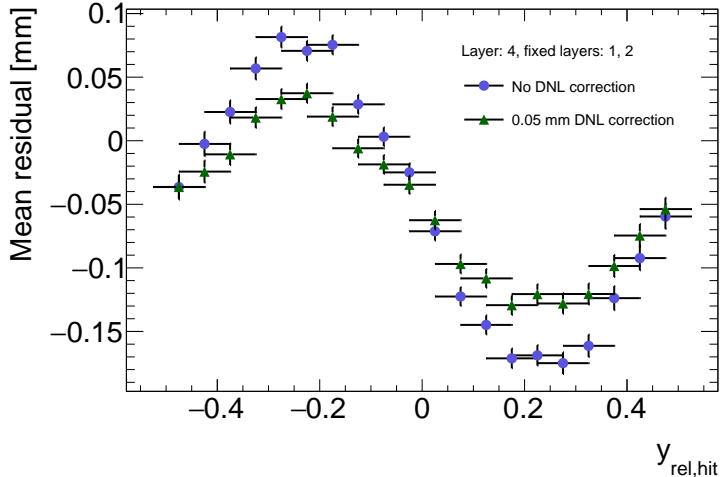


Figure C.6: Effect applying a $50\text{ }\mu\text{m}$ DNL correction to the profile of the residuals sorted by y_{rel} for residuals built from clusters on layers 1 and 2 and extrapolated to layer 4 of quadruplet, QL2.P.8.

mean. The amplitude can be derived by comparing the reconstructed hit position to the expected hit position, as done in [6]. With cosmic muons, there is no reference hit position to compare to, so track residuals were used as a proxy [58]. The hallmark of the DNL effect is the periodic pattern in the residual versus y_{rel} profile, and the effect of correcting the cluster means using an amplitude of $50\text{ }\mu\text{m}$ is shown in Figure C.6. An amplitude of $50\text{ }\mu\text{m}$ is based on Dr. Lefebvre's [58] estimate of the DNL amplitudes by layer, quadruplet and cluster size using cosmic muon tracks [58]. Little variation is seen in the amplitude parameters with respect to the quadruplet tested, the layer and the cluster size so a universal correction is used.

Although the correction is not large enough in this case, the figure shows that the correction does reduce the DNL effect. Slightly better performance is seen in the interpolation tracking combinations where the quality of the residuals is better. DNL corrections for cosmic muon data are difficult because the DNL effect is obscured by the effect of misalignments between strip layers and noise. Misalignments cause the center of the sinusoidal pattern in Figure C.6 to be shifted off of zero, since the mean of residuals is shifted.

Figure C.7 shows the distribution of the difference in residual means calculated in 100 mm by 100 mm areas for mean track residuals on layer 4 obtained using layers 1 and 2 as reference. The mean of the distribution is zero within the root-mean-square so the DNL correction does not bias the residual means. It is apparent that the effect of the DNL correction on

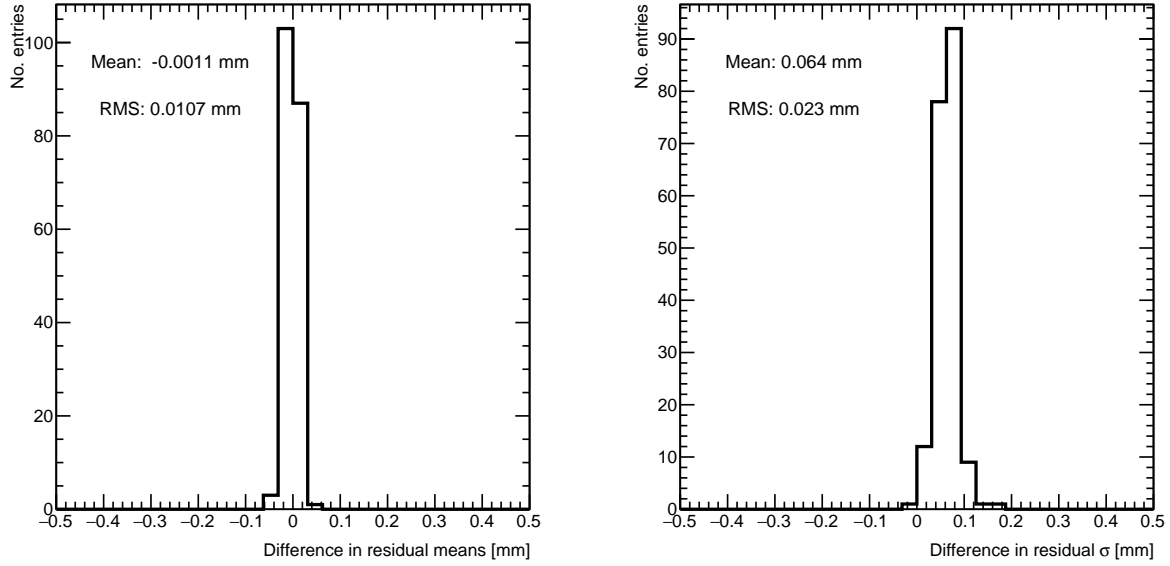


Figure C.7: Difference in residual distribution means and σ 's with and without DNL correction for residuals on layer 4 obtained using reference layers 1 and 2 for sample quadruplet, QL2.P.8.

the residual means is on the order of micrometers given the RMS of $10 \mu\text{m}$ in the worst extrapolation case. Although the σ 's of the residual distributions shrink with the DNL correction, the mean is the parameter of interest so the bias in the fitted σ 's was ignored. Therefore, in this analysis DNL is not corrected for.

₁₄₇₀ Appendix D

₁₄₇₁ Printable plots

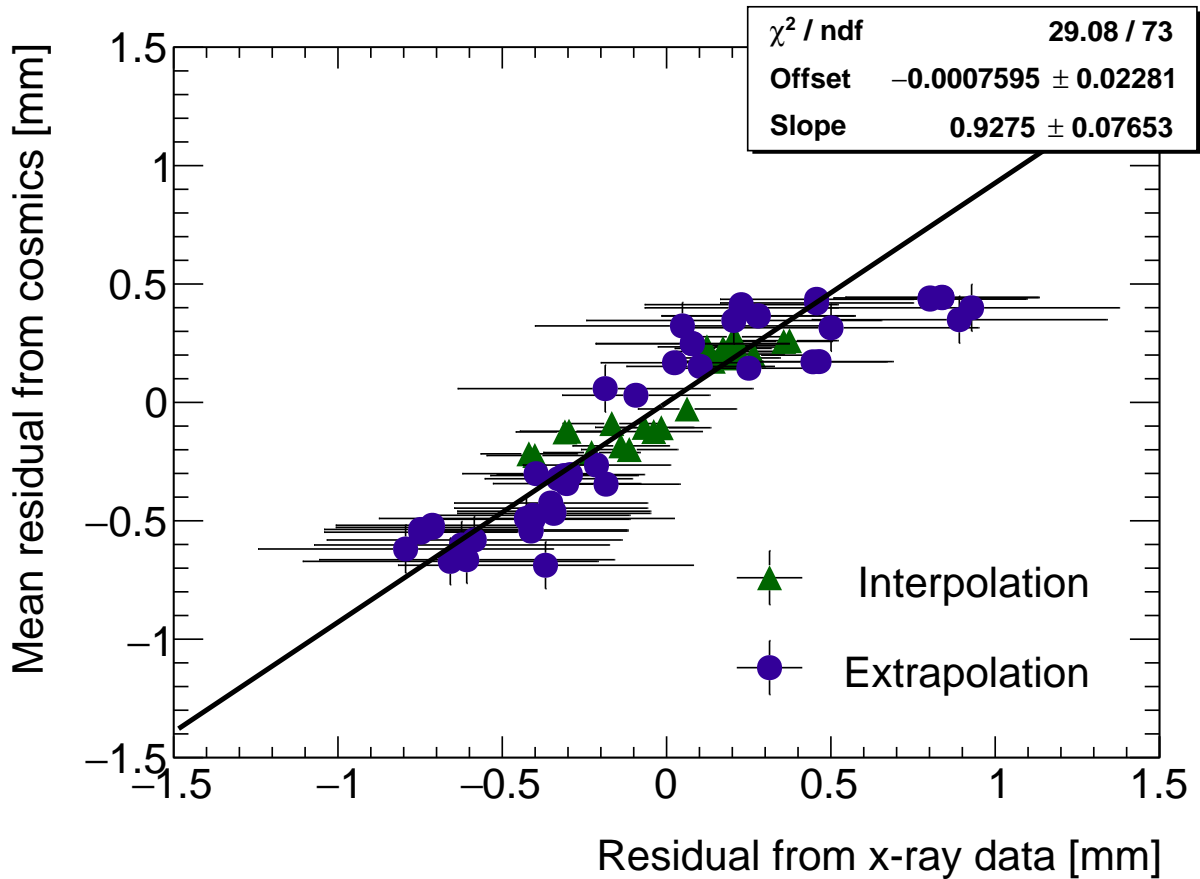


Figure D.1: Correlation plot between x-ray and cosmics residuals for all tracking combinations for QL2.P.11. Each rectangle is centered on an x-ray and mean cosmics residual pair. The width of the rectangles in x and y are the uncertainty in the x-ray and mean cosmics residual respectively. This is a printable version of Figure 7.2 in Section 7.1.

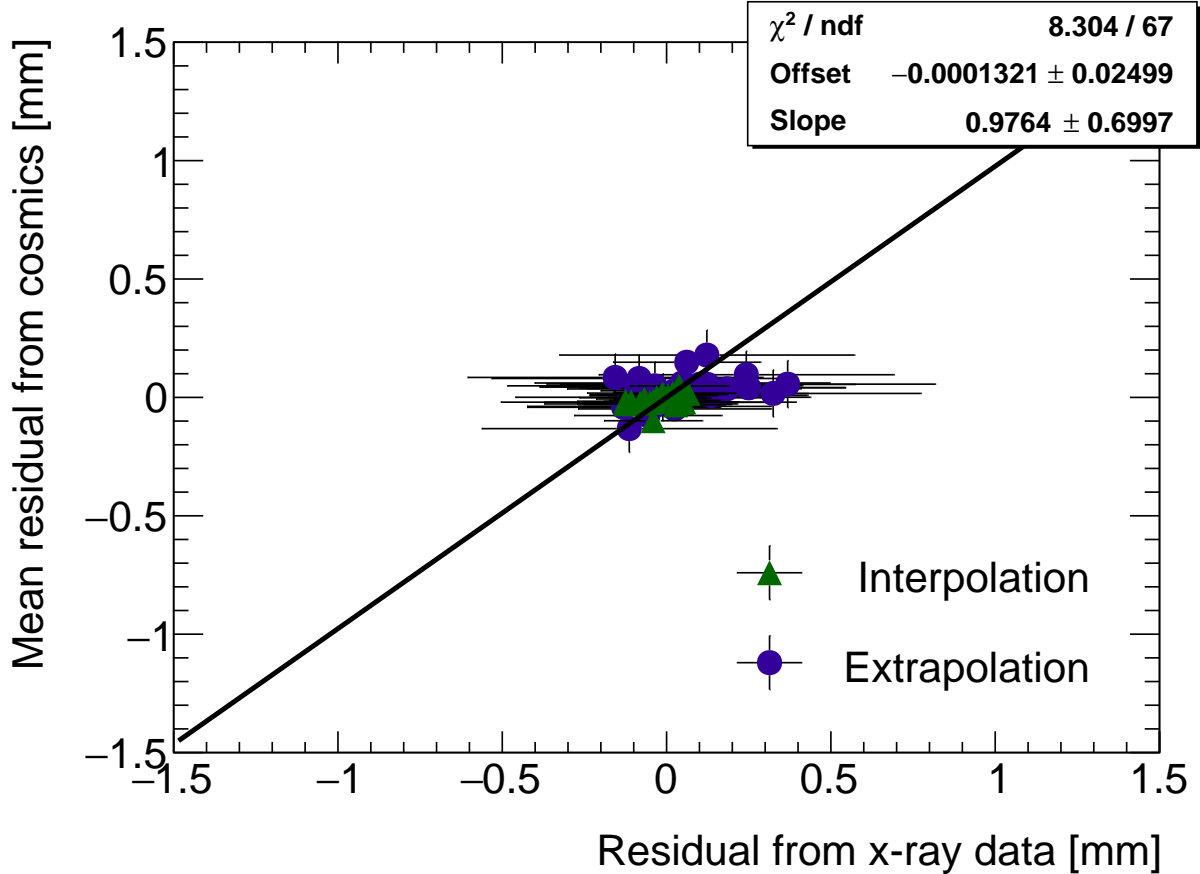


Figure D.2: Correlation plot between x-ray and cosmics residuals for all tracking combinations for QL2.P.8. Each rectangle is centered on an x-ray and mean cosmics residual pair. The width of the rectangles in x and y are the uncertainty in the x-ray and mean cosmics residual respectively. This is a printable version of Figure 7.3 in Section 7.1.